Additive Manufacturing 84 (2024) 104088

Contents lists available at ScienceDirect

Additive Manufacturing

journal homepage: www.elsevier.com/locate/addma

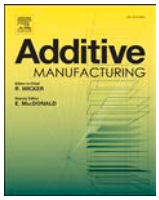

Effect of impinging behavior annular jet shielding gas and printing substrate on metal droplet stable ejection

Yi Zhou, Lehua Qi *, Hongcheng Lian *, Jun Luo, Lin Su

School of Mechanical Engineering, Northwestern Polytechnical University, Xi'an 710072, China

ARTICLE INFO

Keywords:
Coaxial shielding gas
Annular impinging jet
Droplet formation
Metal jet deflection
Metal droplet-based 3D printing

ABSTRACT

Using coaxial shielding gas for low-oxygen protection in metal droplet-based 3D printing helps to promote flexible production and lightweight manufacturing. However, the presence of the printing substrate causes the shielding gas to exhibit complex annular impinging jet characteristics, making the stability of droplet ejection unpredictable. In the present work, the mechanisms of airflow pattern evolution on droplet formation and metal jet deflection were first revealed by incorporating shielding gas simulations, hydrodynamic modeling, and droplet ejection experiments. An innovative airflow disturbance suppression strategy for metal droplet ejection was proposed, which can remarkably reduce the shielding gas disturbance on droplet printing. Results show that the change in deposition distance leads to a transition between two typical airflow patterns, thus affecting the droplet ejection behavior. When the deposition distance exceeds 2.5 mm, metal jets would be stretched even to a secondary break under airflow pattern 1, accelerating droplets. For the deposition distance below 2.5 mm, metal jet shortening and droplet deceleration would occur under airflow pattern 2, deflecting jet trajectory. The negative airflow effect on droplet ejection could be avoided by controlling the deposition distance to the transition region of two airflow patterns. Furthermore, a ball grid array (BGA) chip ball-mounting and two thin-wall tube printing were realized based on metal droplet ejection in annular impinging jet shielding gas. This work provides theoretical and technical guidance for the stable ejection and accurate printing of metal droplets in an opening low-oxygen environment.

1. Introduction

Metal droplet-based 3D printing is a novel metal additive manufacturing technology that uses micron-sized molten droplets as forming units [1]. The technology has no special requirements for the shape and size of the raw material, as a melt block is sufficient for droplet ejection. It also does not require any high-power energy sources such as lasers, arcs, ion beams, etc. Compared with other metal additive manufacturing processes such as selective laser melting (SLM), electron beam selective melting (EBSM), and laser engineered net shaping (LENS), the technology has the advantages of low heat input, no need for unusual raw materials, and low energy consumption. It is a promising method for small and complex metal parts fabrication [2], electronic packaging [3], and in-situ structural repair [4].

Since the oxidation of metal melt could affect printing quality, it is necessary to provide low-oxygen protection during metal droplet ejection. The closed low-oxygen atmosphere commonly used in metal droplet-based 3D printing, such as the inert gas glove box, hinders the rapid material delivery and is unsuitable for the lightweight manufacturing. Coaxial gas blowing is an opening low-oxygen protection strategy in several additive manufacturing fields, such as laser-assisted directed energy deposition (L-DED) [5], melt blowing (MB) [6], and gas atomization (GA) [7]. Metal droplet 3D printing with coaxial shielding gas enables rapid material delivery and the real-time processing of large parts, making it more applicable to the intelligent, automated, and lightweight industrial environment. Unlike other shielding gas solutions, such as the lateral gas blowing method [8,9] and the StarJet nozzle [10,11], in the coaxial gas blowing configuration, the airflow supply direction is consistent with the droplet ejection direction, resulting in less lateral airflow disturbance and a longer low-oxygen protection distance. Over the past few decades, studies on metal droplet-based 3D printing in a closed low-oxygen atmosphere have been well-established for various metal materials (e.g., tin [12], copper [13], aluminum [14], platinum [15], and gold [16]) and numerous applications (e.g., 3D part printing [17], thin-wall forming [18], circuit fabrication [19], solder ball preparation [20], and circuit bonding [21]).

* Corresponding authors.
E-mail addresses: qilehua@nwpu.edu.cn (L. Qi), hongchenglian@nwpu.edu.cn (H. Lian).

https://doi.org/10.1016/j.addma.2024.104088
Received 14 November 2023; Received in revised form 1 February 2024; Accepted 16 March 2024
Available online 19 March 2024

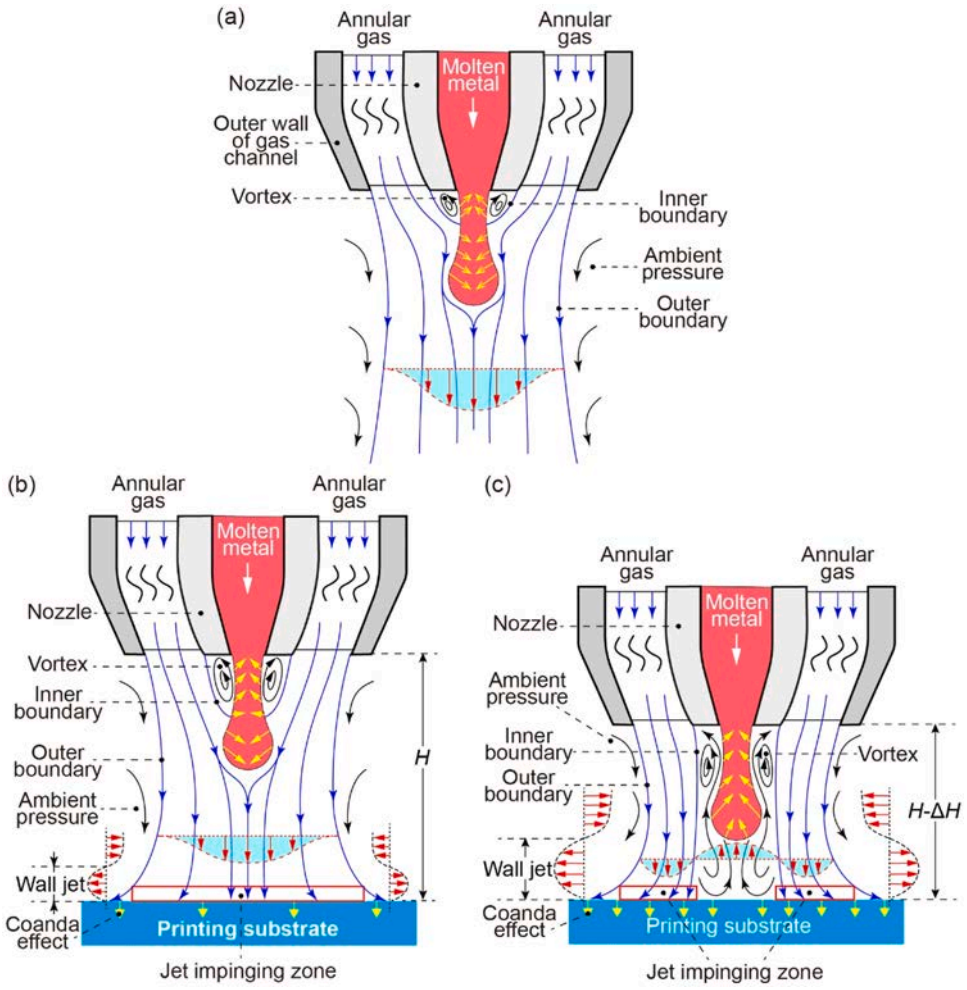

Fig. 1. (a) Schematic diagram of an annular free jet. Annular impinging jets at a (b) longer and (c) closer deposition distance of the printing substrate.

However, new problems might be posed when applying coaxial shielding gas in metal droplet printing due to the complex gas flow behavior. The industrial application for the relevant technology still requires an essential improvement in the theoretical guidance of the printing process.

Several researchers have theoretically investigated the metal droplet ejection process under shielding gas. Amirzadeh et al. [22] investigated the effect of the shielding gas supply pressure on the droplet diameter and the jet break number. Zhou et al. [23] analyzed the effect of oxidation on droplet morphology and the effect of airflow vortex on satellite droplet formation. These studies are all based on the shielding gas free jet since the neglect of the substrate influences on the printing process. The flow field structure for an annular free jet is shown in Fig. 1 (a). When the annular free jet flows out from the nozzle, the annular airflow affected by the ambient pressure bends toward the central axis and merges due to the Bernoulli effect. At the same time, the sudden cut-off of the flow channel creates a vortex at the nozzle outlet [24,25], so that the root and front of the metal jet are pushed in different directions by the airflow. However, due to the direct impingement between the airflow and the substrate in the actual printing process, the blocking of the printing substrate makes the shielding gas a complex impinging jet instead of a free jet. The Coanda effect of the substrate would create a wall jet, which hinders the converging behavior of the annular jet and changes the vortex range near the nozzle, as shown in Fig. 1(b). As the deposition distance decreases, the substrate influence on the airflow intensifies, leading to significant changes in the vortex region and the force on metal jets (Fig. 1(c)) [26]. Due to the small size characteristic and slow ejection velocity of metal droplets, the airflow behavior at different deposition distances would affect the ejection behavior of metal droplets, causing the ejection stability and printing accuracy of metal droplets in the annular impinging jet shielding gas to be unpredictable. Meanwhile, the narrow flow space of shielding gas makes it challenging to observe the airflow pattern. Therefore, it is meaningful to investigate the flow dynamic mechanism of annular impinging gas on metal droplet ejection for relevant technology promotion.

In this work, based on the effect mechanism research of annular impinging jet shielding gas on metal droplet ejection, an innovative suppression strategy of airflow disturbance for the droplet stable ejection and accurate printing was proposed. A metal droplet ejection experiment, an airflow simulation based on the Reynolds stress model, and a hydrodynamic model for droplet ejection were combined to reveal the airflow dynamic effect on droplet formation and metal jet deflection. Techniques such as high-speed photography and smoke-line airflow tracing were employed to capture the practical airflow trace and the droplet transient information. Finally, a ball grid array (BGA) chip ball-mounting and two thin-wall tube printing were realized by droplet direct printing in an opening low-oxygen protective environment, demonstrating the research practicability for engineering applications. This study could provide theoretical and technical guidance for the stable ejection and accurate printing of metal droplets in an opening low-oxygen environment.

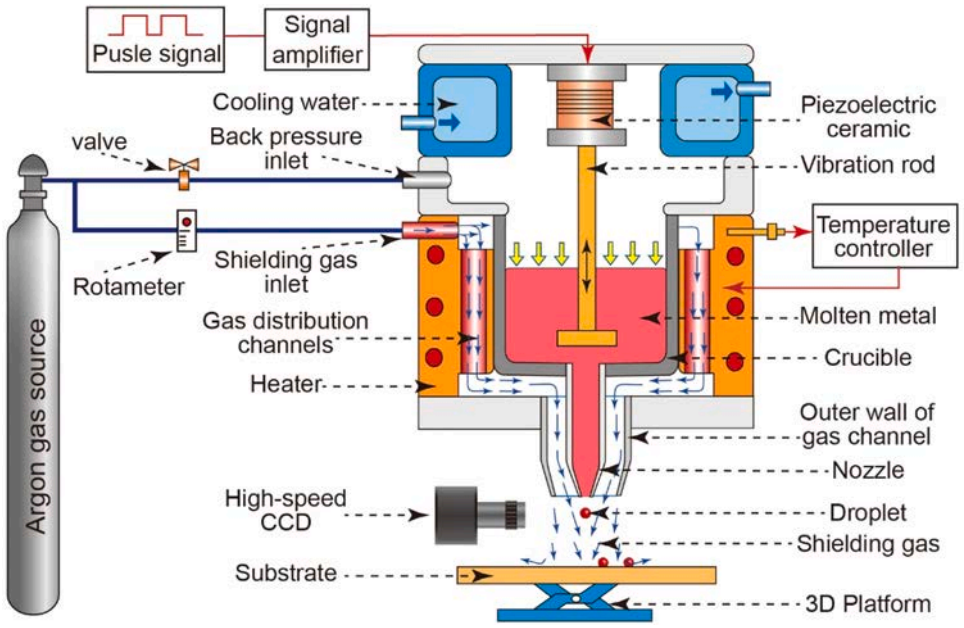

Fig. 2. Schematic diagram of metal droplet printing platform.

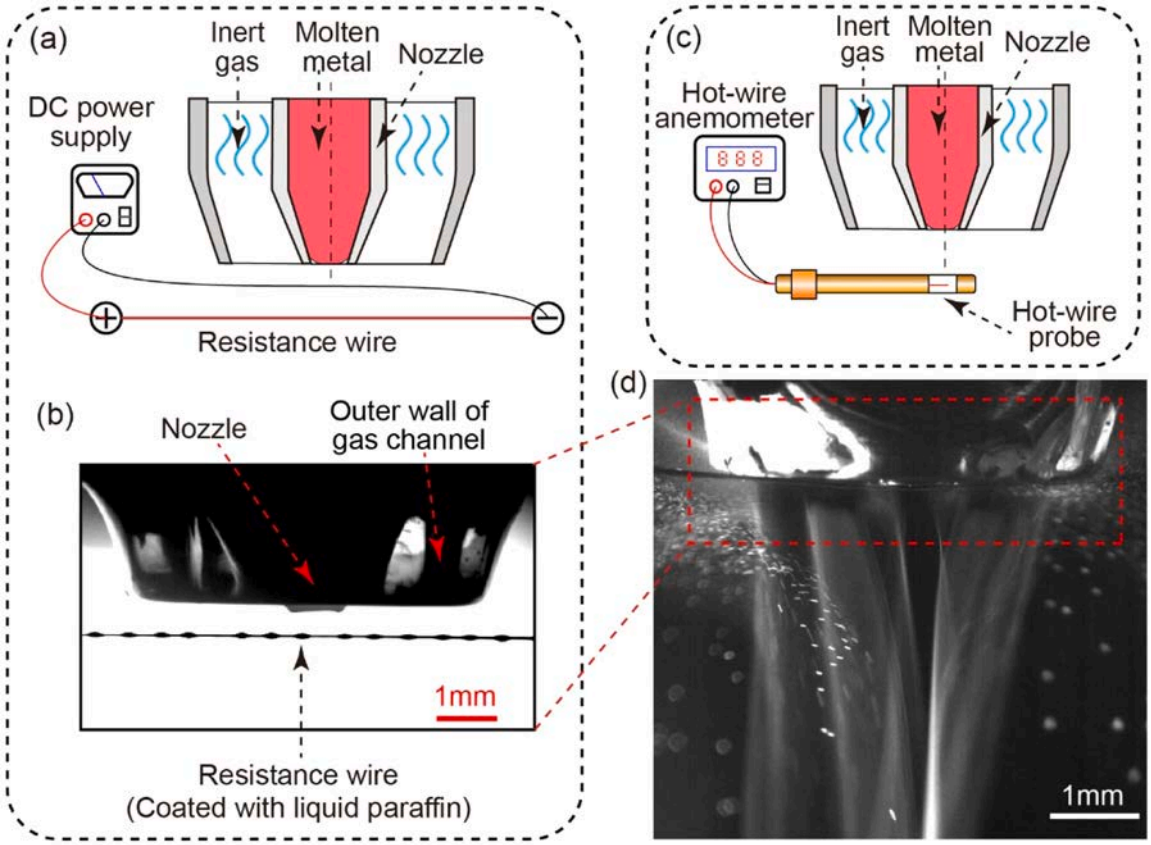

Fig. 3. Schematic diagram of (a) smoke-wire technique application and (c) hot-wire anemometer application. Experimental diagram of (b) smoke-wire technique application and (d) practical airflow trace captured.

2. Methodologies

2.1. Experimental setup

A schematic diagram of the metal droplet printing platform is shown in Fig. 2, which mainly consists of a temperature control subsystem, a metal droplet ejection subsystem, a motion control subsystem, and an inert gas supply subsystem. The experimental system works as follows. First, metal blocks are heated and melted in a crucible via a temperature controller (Shimax, Japan), a type K thermocouple, and a heater. In the

Table 1
Properties of materials used in the simulation and experiment.

Properties	Sn99.3-Cu0.7	argon
Density (kg·m^{-3})	ρ_m=6900	ρ_g=1.6228×10^{-3}
Dynamics viscosity (Pa·s)	μ_m=1.4×10^{-3}	μ_g=2.125×10^{-5}
Surface tension coefficient (N·m^{-1})	σ=0.55	-
Thermal conductivity (W·m^{-1}·K^{-1})	k_m=16.5	k_g=0.017
Specific heat (J·kg^{-1}·K^{-1})	C_m=243.36	C_g=521

metal droplet ejection subsystem, an ejection pulse signal set by a signal amplifier (Coremorrow, XE-505.00, China) acts upon a piezoelectric ceramic (Coremorrow, China), which converts the electrical energy into mechanical energy to drive the oscillation of a vibration rod. Then, a metal droplet could be ejected from the nozzle. With the synchronous control of the motion control subsystem (PMAC, Delta Tau, America), a three-dimensional motion platform regulates the distance and position of metal droplet deposition by translating and lifting a substrate. During the printing process, cooling water is continuously circulated around the piezoelectric ceramic to prevent performance degradation caused by the exceeding the Curie temperature. The inert gas supply subsystem provides a localized low-oxygen environment and a back pressure, which is necessary for the anti-oxidation and the waste squeezing of the melt.

A self-developed annular shielding gas supply structure was employed to create the micro-domain protective environment. The gas inlet is located at the top of the heater. Shielding gas is delivered to the nozzle through gas distribution channels around the inner wall of the heater, preventing the molten jet from cooling by the lower temperature airflow and improving airflow uniformity. An extended and thin annular configuration near the nozzle ensures the shielding gas flow downward vertically. Additionally, the nozzle front has a slight gradual 15° contraction angle to prevent airflow diffusion.

A smoke-wire (SW) technique was employed to capture practical airflow traces. Fig. 3(a) and (b) show a schematic diagram and an experimental diagram of the smoke-wire technique application method, a 0.1 mm diameter NiCr resistance wire is placed between the nozzle and the substrate. Each time before testing the airflow pattern, the resistance wire is coated with paraffin oil. The Joule effect of the resistance wire produces visible airflow smoke (as shown in Fig. 3(d)) when a DC power supply is energized. Besides, a hot-wire anemometer (Jiahan, W410D2, China) was used to measure the shielding gas velocity, as shown in Fig. 3(c). When the airflow passes through the hot-wire probe, the heat dissipation changes the hot-wire resistance and converts airflow velocity signals into electrical signals. Because of the narrow space at the gas outlet, there might be a large error if the airflow velocity is measured directly. Therefore, before measuring the airflow velocity, shielding gas is driven to pass through a circular tube with the same cross-sectional area as the gas outlet. By comparing the practical airflow velocity controlled by a rotameter with the anemometer-measured velocity, a correction coefficient for the measured velocity could be obtained.

Droplet dynamic processes and airflow smoke trails were recorded by a high-speed CCD camera (ix-speed 220, Britain) with a frame rate of 9500–10,000 f/s. Metal droplet solidification morphologies were visualized by a scanning electron microscope (Zeiss, EVO 10, Germany). The feature size measurement of metal jets and droplets was performed by an image analysis software (Image J). To capture a clearer shielding gas smoke trajectory and a more stable droplet ejection process, 300 μm diameter droplets were used in this paper. In addition, Sn99.3-Cu0.7 was used as the printing material, and argon was used as the shielding gas. When the metal jet oxidizes, it breaks up to form a droplet with a characteristic tail due to decreased surface tension and increased viscosity [23,27]. To prevent the oxide skin formation, whether or not to form trailing droplets was regarded as the judgment basis, the shielding gas supply rate was controlled to be over 1.2 L/min.

The physical properties of argon and Sn99.3-Cu0.7 alloy at 623 K are shown in Table 1 [28–32].

2.2. Numerical approach

2.2.1. Governing equations

To obtain an insight into shielding gas flow characteristics, the airflow behavior is simulated based on the Reynolds stress model (RSM). The transport equation of the RSM is derived by multiplying the Reynolds mean of the momentum equation by the velocity fluctuations, making it more accurate than the popular k-ε model. Krutka et al. [33] found that the RSM model is more suitable than the k-ε model for the simulation of double-slit jets. Moore et al. [24] used the parameters proposed by Krutka et al. to simulate annular melt-blown dies, finding that the average axial velocity in the simulation was in good agreement with the experimental data.

The mathematical model is based on several assumptions and simplifications as follows: (1) the shielding gas is a continuous and incompressible fluid medium during the flow; (2) the initial shielding gas velocity is a uniformly distributed plug flow at the inlet; (3) the shielding gas is an ideal gas with constant viscosity because of the nearly isothermal nature of the airflow.

For steady-state and isothermal conditions, the Reynolds stress transport equation is

$$\frac{\partial}{\partial x_k}\left(\rho_g U_k \overline{u_i u_j}\right) = -\frac{\partial}{\partial x_k}\left[\rho_g \overline{u_i u_j u_k} + \overline{\rho_g\left(\delta_{kj}u_i + \delta_{ik}u_j\right)}\right] + \frac{\partial}{\partial x_k}\left[\mu_g \frac{\partial}{\partial x_k}\left(\overline{u_i u_j}\right)\right] - \rho_g\left(\overline{u_i u_k}\frac{\partial U_j}{\partial x_k} + \overline{u_j u_k}\frac{\partial U_i}{\partial x_k}\right) + \overline{P_g\left(\frac{\partial u_i}{\partial x_j} + \frac{\partial u_j}{x_i}\right)} - 2\mu_g \overline{\frac{\partial u_i}{\partial x_k}\frac{\partial u_j}{\partial x_k}} \tag{1}$$

where U_i, U_j, and U_k are the velocity components in directions i, j, and k, respectively; $\overline{u_i}$, $\overline{u_j}$, and$\overline{u_k}$ are the time-averaged velocity

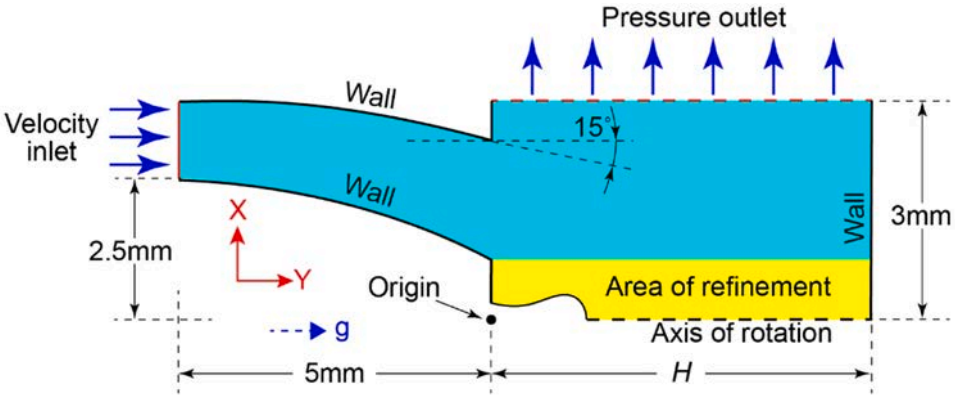

Fig. 4. Computational domain structure used in the simulation. The figure is rotated 90° relative to the actual airflow field.

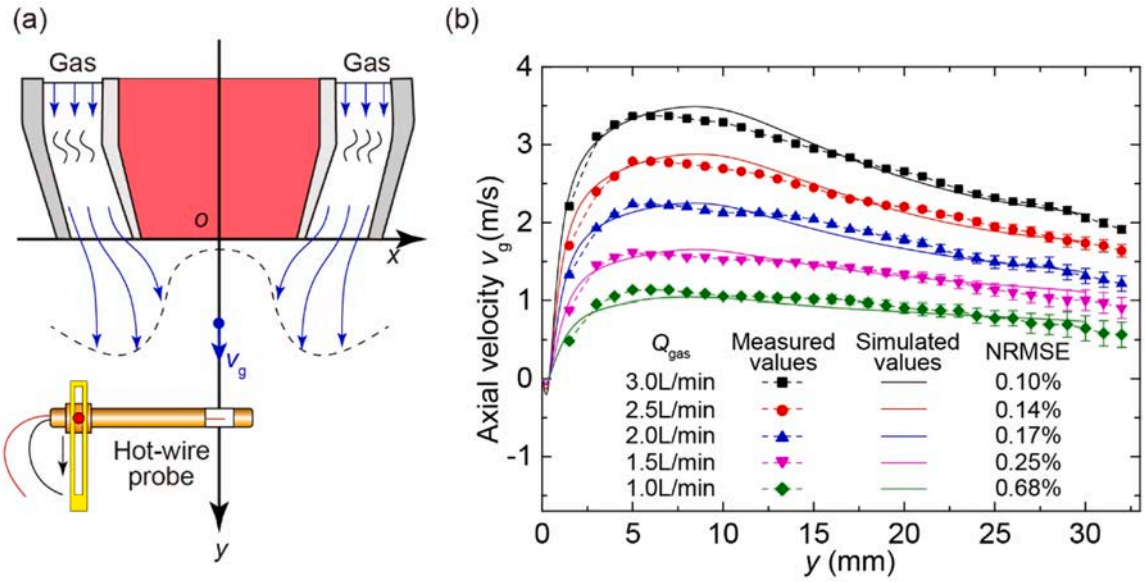

Fig. 5. (a) Schematic diagram of the shielding gas velocity measurement position. (b) Shielding gas axial velocity comparison in the simulation and experiment.

components in directions i, j, and k, respectively; x_i, x_j, and x_k are the spatial coordinates in directions i, j, and k, respectively; P_g is the pressure of the gas; δ_{kj} is the Kronecker function, i.e.$\delta_{kj} = 1(k = j), \delta_{kj} = 0(k \neq j)$.

Except for the Reynolds stress transport equation, the dissipation rate is calculated via the standard k-ε model as

$$\rho_g \frac{D\varepsilon}{Dt} = \frac{\partial}{\partial x_i}\left[\left(\mu_g + \frac{\mu_t}{\sigma_\varepsilon}\right)\frac{\partial \varepsilon}{\partial x_i}\right] + C_{1\varepsilon}\frac{\varepsilon}{k}G_k - C_{2\varepsilon}\rho_g\frac{\varepsilon^2}{k} \quad (2)$$

where t is the time; μ_t is the turbulent viscosity; G_k is the turbulent kinetic energy; $C_{1\varepsilon}$, $C_{2\varepsilon}$ are empirical constants; And σ_ε is the turbulent Planter constant for the turbulent dissipation rate ε.

2.2.2. Geometric model

The simulation of shielding gas flow behavior was based on the computational domain structure shown in Fig. 4. In the airflow computational domain, the coordinate system origin is located at the center of the nozzle bottom surface. The positive y-axis is parallel to the gravity acceleration direction, and the positive x-axis is perpendicular to the gravity acceleration direction. The total width of the entire computational domain is 3 mm, which is sufficient to define shielding gas's radial development. The annular shielding gas (2.5 mm for the inner diameter and 3 mm for the outer diameter) flows into the computational domain from the left inlet. After a 5 mm tapered channel delivery, the annular jet shielding gas actively developed in a region with a length of H, eventually radially flowing out of the computational domain. In addition, for axisymmetric flow problems, a two-dimensional axisymmetric computational domain was used to reduce the simulation time. In contrast, a three-dimensional computational domain was used for non-axisymmetric flow problems.

2.2.3. Mesh and boundary conditions

Quadrilateral meshes were used to solve the two-dimensional computational domain, while hexagonal meshes were used to solve the three-dimensional computational domain. Considering that the droplet ejection process is mainly affected by the shielding gas near the central axis, the grid refinement was performed near the central axis to improve the calculation accuracy. The minimum grid size after densification could reach 15 μm. The shielding gas inlet and outlet are defined as velocity inlet and pressure outlet, respectively. The remaining boundaries, including the airflow channel, the printing substrate, and the droplet transient contour, were defined as no-slip walls. After about 5000 iterations, the calculation results tend to converge.

2.2.4. Numerical model validation

The effect of metal jet transient evolution on shielding gas was ignored in the simulation, and the calculation was performed only for the steady-state flow field of shielding gas. The adjusted model constants based on that of Krutka et al. were used, i.e., $C_{1\varepsilon}$=1.1, $C_{2\varepsilon}$=2.05, and σ_ε=1. As shown in Fig. 5(a), a corrected hot-wire anemometer was used to measure the airflow velocity at the nozzle exit. Moreover, to evaluate the precision of the simulation, the normalized root mean squared error (NRMSE) is obtained by using NRMSE $= \|y^e - \hat{y}^e\|/\|y^e\|$[34], where y^e is the experimental value and $\hat{y}^e$is the simulation value. Fig. 5(b) compares the axial velocity of shielding gas in the simulation and experiment. For different supply rates of shielding gas, Q_{gas}, the axial velocity of shielding gas is well-matched between the RSM calculation and the experimental measurement, while the maximum NRMSE between the experimental and the simulated data is only 0.68%, demonstrating that the simulation model has high reliability.

2.3. Hydrodynamic modeling

Metal droplet ejection under shielding gas is a complex gas-liquid-solid coupling process influenced by many factors, such as shielding gas flow characteristics, crucible structure, material properties, and vibration element motion characteristics. An effective physical model would help understand the parameter relationship between shielding gas and droplet ejection. There are two common approaches to building a physical model. One is a mechanism model based on underlying physical principles and mathematical modeling methods, and the other is a data-driven model based on machine learning techniques and data analysis methods. It has been demonstrated that the data-driven model has advantages in reducing the computation burden and improving the computation accuracy, for example, L. J. Segura et al. [35,36] used a neural network algorithm to model the inkjet printing process and investigate the ejection dynamics, which achieved the accurate prediction of the droplet ejection behavior. However, in this study, it is hard to build a data-driven model due to the lack of sufficient sample data. To reveal the fundamental principles and causal relationships of the metal droplet ejection system under shielding gas, a mechanism model based on hydrodynamics is appropriated to analyze the droplet ejection

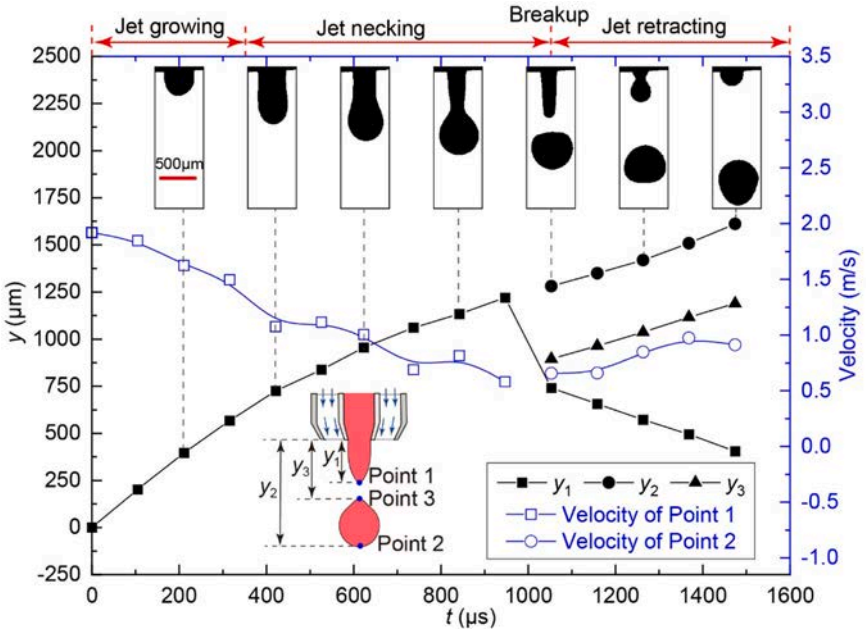

Fig. 6. Experimental results of a single tin alloy droplet ejection process in free jet shielding gas with a low gas supply rate of 1.2 L/min.

process.

Several essential stages, such as jet growing, jet necking, jet breakup, and jet retracting, are divided during droplet formation [37]. Fig. 6 shows the experimental results of a single tin alloy droplet ejection in free jet shielding gas for Q_{gas}=1.2 L/min. During 0 μs~347 μs after an ejection signal is applied, molten metal is ejected from the nozzle and continuously grows into a metal jet due to the forward motion of the vibration rod. The jet tip rapidly shrinks to a spherical shape under surface tension. During 347 μs~1050 μs, with the disappearance of the ejection signal, the jet velocity in the root decreases as the vibration rod moves back. A jet necking occurs due to the velocity difference between the jet root and the jet tip. Then the jet tip breaks up when the metal jet grows to about 1.23 mm at 1050 μs, producing a single metal droplet. After 1050 μs, the remaining metal jet is pulled back into the nozzle by viscous tension and surface tension, completing a droplet ejection cycle. During jet breaking, the velocities of Point 1 at the jet tip and Point 2 at the droplet front show that the metal jet has an initial velocity of approximately 1.8 m/s, and the droplet has an initial velocity of 0.8 m/s due to the effects of surface tension and viscous tension.

The visual presentation of the metal droplet ejection process under shielding gas is shown in Supplementary Video 1.

The flow of shielding gas would accelerate the cooling of droplets and change material properties. It is essential to determine the influence of airflow on droplet temperature variation. The Biot number, defined as the product of the convective heat transfer coefficient and the droplet characteristic size divided by the droplet thermal conductivity (hD_d/k_m), is commonly used to evaluate the temperature gradient inside droplets. Where the convective heat transfer coefficient (h) for spherical droplets is given by the Ranz-Marshall correlation [38]

$$h = \frac{k_g}{D_d}\left(2 + 0.6 Re_g^{1/2} Pr_g^{1/3}\right) \tag{3}$$

Re and Pr are the Reynold number and the Prandtl number of the shielding gas, expressed by $Re_g = v_g D_d \rho_g / \mu_g$ and $Pr = C_g \mu_g / k_g$. Here k_g,

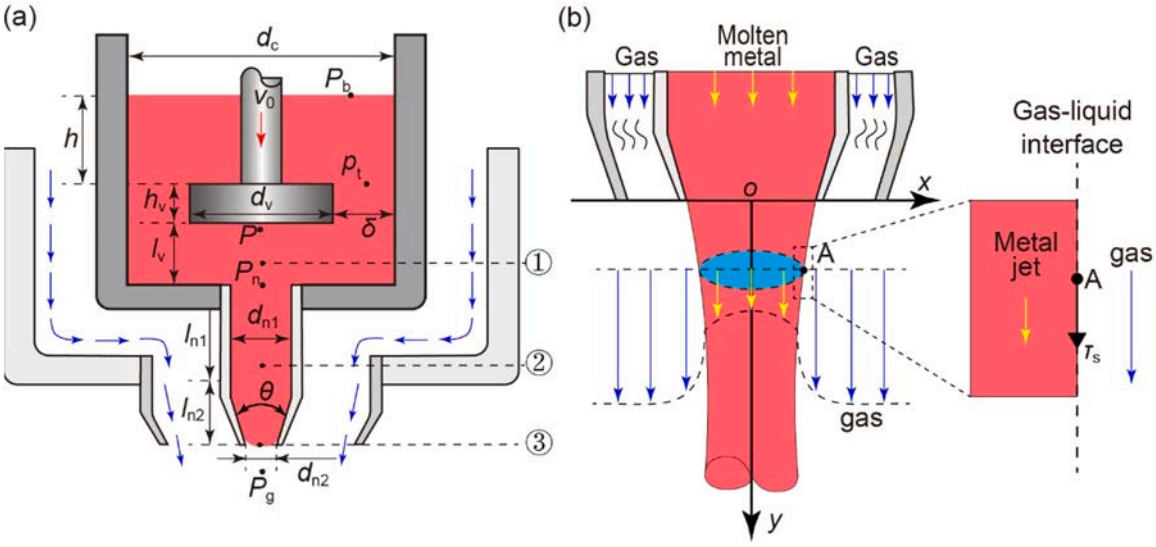

Fig. 7. Physical model schematics of (a) droplet ejection in the shielding gas environment and (b) the shear force in gas-liquid interface.

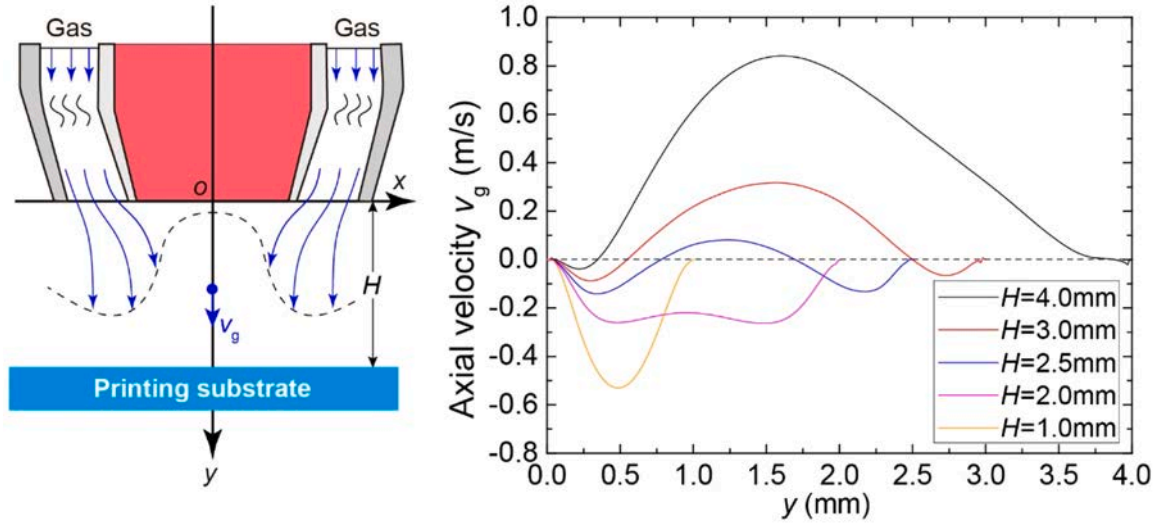

Fig. 8. Simulation results of the axial velocity of the annular impinging jet shielding gas at different deposition distances. The shielding gas supply rate Q_{gas} is 3 L/min.

v_g, ρ_g, μ_g, and C_g are airflow thermal conductivity, velocity, density, viscosity, and specific heat, respectively. In the experiment, the flow rate of the shielding gas doesn't exceed 5 m/s, while the droplet diameter is ~400 μm. It could be calculated that the convective heat transfer coefficient is ~93.637 $W{\cdot}m^{-2}{\cdot}K^{-1}$, while the Biot number is ~0.002. The temperature gradient inside droplets could be neglected as the Biot number is less than 0.01 [39]. The droplet temperature is much higher than the ambient temperature during the ejection process. The heat is transferred from the droplet to the atmosphere mainly by convection and radiation. From Newton's law of cooling, the cooling rate of a spherical droplet is [40] :

$$\frac{dT}{dt} = -\frac{6\left[h\left(T-T_g\right)+\sigma_{SB}\varepsilon_e\left(T^4-T_g{}^4\right)\right]}{\rho_m C_m D_d} \tag{4}$$

Where T and T_g are the initial temperatures of droplets and shielding gas; ρ_m and C_m are the droplet density and specific heat; σ_{SB} is the Stefan-Boltzmann constant; ε_e is the emissivity. At $T = 623$ K and $T_g = 300$ K, the calculated droplet cooling rate is ~270 $K{\cdot}s^{-1}$. According to the experiment, the flight time of the droplet before reaching the substrate should not exceed 2 ms, which causes a temperature loss of <1 K. Therefore, the temperature decrease caused by the shielding gas during droplet ejection is neglected in this paper.

Assume that the molten metal is an incompressible, continuous, and homogeneous Newtonian fluid. As shown in Fig. 7(a), a physical model has been established based on the mechanism of metal droplet ejection in shielding gas. v_0 is the forward velocity of the vibration rod; d_c, d_v, d_{n1}, and d_{n2} are the diameters of the crucible, rod head, nozzle straight section, and nozzle outlet, respectively; h is the distance from the top surface of the molten metal to that of the vibration rod; h_v is the thickness of the rod head; P_b is the back pressure of the molten metal; P_t, P, P_n, and P_a are the pressures on the rod head top surface, the rod head bottom surface, the nozzle inlet, and the atmosphere, respectively; δ is the width of the annular lateral gap between the rod head and the crucible; l_v, l_{n1}, and l_{n2} are the lengths of the vibration chamber, the nozzle straight section, and the nozzle constriction section, respectively (positions ①~③ as shown in Fig. 7(a)); and θ is the angle of the nozzle constriction section.

A more detailed process of the model construction is given in Appendix A. For a molten metal with a density ρ_m and a dynamic viscosity μ_m, the metal jet ejection velocity, v_3, can be calculated based on the fluid mechanics theory, as

$$v_3 = -\frac{B}{2A}+\frac{\sqrt{B^2+4AC-4AP_a}}{2A} \tag{5}$$

Here, $A = 0.21\rho_m {d_{n2}}^4/{d_{n1}}^4(1-{d_{n1}}^2/{d_c}^2)+0.02\rho_m$, $B = 32\mu_m {d_{n2}}^2({l_v}/{d_c}^4+{l_{n1}}/{d_{n1}}^4)+3\mu_m h_v {d_{n2}}^2/d_v\delta^3$, and $C = 3\mu_m h_v/\delta^3(d_v v_0+2v_0\delta)+\rho_m g(l_v+l_{n1}+l_{n2}+h)+P_b-2\sigma/d_{n2}$.

Eq. (5) shows that an increase in the ambient pressure will cause a decrease in the ejection velocity of metal jets. The ambient pressure approaches zero at a low shielding gas flow rate. In this situation, the jet ejection velocity from Eq. (5) is 1.7 m/s, which is very close to the measured velocity of 1.8 m/s.

Assuming that the driving signal disappears at time t_1, the jet breaks up at time t_2. The initial velocity of the droplet, v_d, was obtained by the momentum conservation model of jet ejection (see Appendix A for details). v_d is expressed by the metal jet ejection velocity v_3 and the average velocity of shielding gas $\overline{v_g}$ as

$$v_d = \frac{D{v_3}^2+Ev_3\overline{v_g}\left|\overline{v_g}\right|-F}{G-H\overline{v_g}\left|\overline{v_g}\right|} \tag{6}$$

Here, $D = 3\rho_m {d_{n2}}^2 t_1$, $E = 2f_s\rho_g d_{n2}t_2{}^2$, $F = 9\mu_m {d_{n2}}^2+2d_{n2}\sigma t_1+4d_{n2}\sigma t_2$, $G = 2{d_d}^3\rho_m$, and $H = f_s\rho_g d_{n2}t_2{}^2$. f_s is the shear factor, and d_d is the droplet diameter.

The jet break length, l_b, is expressed as

$$l_b = \int_0^{t_2}\left(v_3+\frac{v_d-v_3}{t_2}t\right)dt = \frac{1}{2}\left(v_3+v_d\right)t_2 \tag{7}$$

From (5); (6); (7), an increase in gas velocity increases the initial velocity of droplets and the break length of jets, while an increase in ambient pressure decreases them.

3. Results and discussion

3.1. Flow properties of the annular impinging jet shielding gas

In an annular free jet, the airflow field could be divided into three regions according to the flow behavior on the axis: recirculation zone, transition zone, and established-flow zone [41]. The recirculation zone is formed at the nozzle outlet due to the central-wall effect caused by the sudden cut-off of the airflow channel, where the airflow direction is opposite to the gas supply direction. As the annular airflow gradually converges toward the central axis, the airflow axial velocity gradually increases, forming the transition zone. In the established-flow zone, the

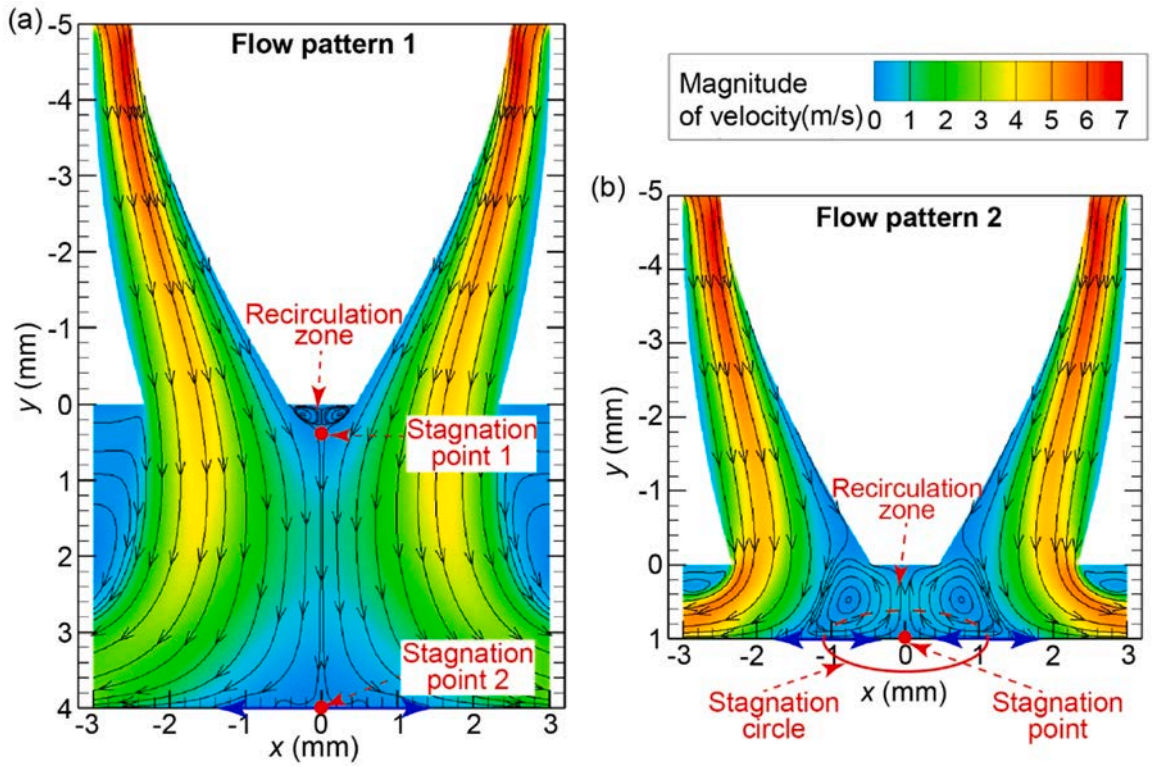

Fig. 9. Velocity contour and streamline of two typical flow patterns at different deposition distances: (a) 4 mm; (b) 1 mm. The shielding gas supply rate Q_{gas} is 3 L/min.

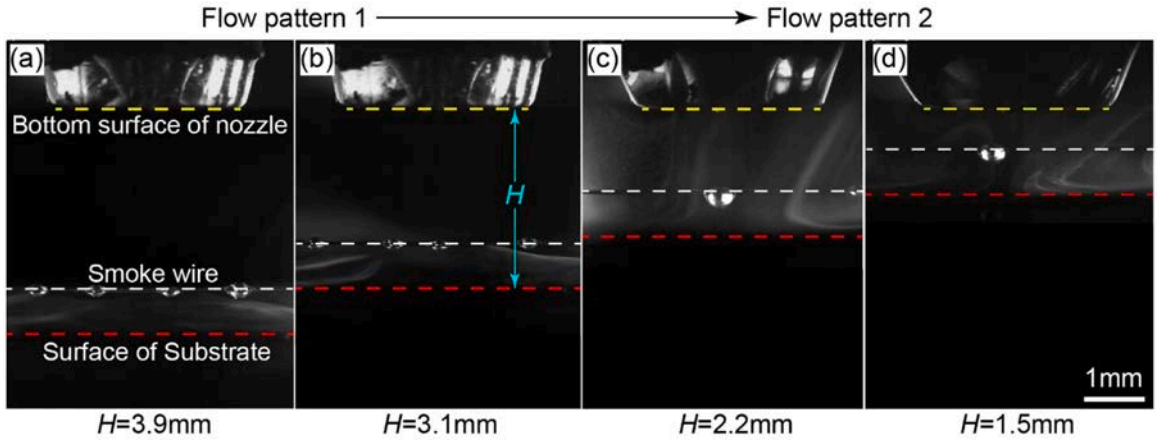

Fig. 10. Airflow smoke trajectories at different deposition distances: (a) 3.9 mm; (b) 3.1 mm; (c) 2.2 mm; (d) 1.5 mm. The shielding gas supply rate Q_{gas} is 3 L/min.

airflow kinetic energy would be gradually reduced by external gas until it merges with the atmosphere. In an annular impinging jet, the substrate blocking effect can influence the formation size of the recirculation zone and further change the droplet ejection behavior.

Fig. 8 shows the axial velocity simulation results of the annular impinging jet shielding gas at different deposition distances. When the deposition distance H is farther than 2.5 mm, a small size recirculation zone forms at the nozzle outlet. Due to the strengthening of the airflow convergence ability, the peak value of the airflow axial velocity, v_g, obviously increases with the increase of H and then gradually decreases to zero near the blocking substrate. On the other hand, only reverse airflow exists when H is less than 2.5 mm, and the trough value of v_g decreases with the decrease of H. Thus the flow characteristics of shielding gas at different deposition distances can be divided into two patterns [42]. One is that airflow transits from reverse flow to positive flow at a farther deposition distance, the other is that the reverse flow fills the entire deposition space at a smaller deposition distance.

From Fig. 8, the transition of two airflow patterns occurs near a deposition distance of 2.5 mm. To illustrate the airflow structure of two typical airflow patterns, the velocity contour and streamline at 4 mm and 1 mm deposition distances were chosen. In flow pattern 1 (Fig. 9 (a)), the remote substrate has little influence on the formation of the airflow recirculation zone, while the continuous change of the airflow direction along the central axis leads to two airflow stagnation points in the flow field. When gas flows out of the annular channel, the annular airflow can overcome the nozzle central-wall effect and converge to the central axis under the Bernoulli effect. In contrast, in flow pattern 2, the adjacent substrate plays a more important role in the formation of the airflow recirculation zone. The Coanda effect of the substrate suppresses the convergence of the annular gas, causing the airflow to directly

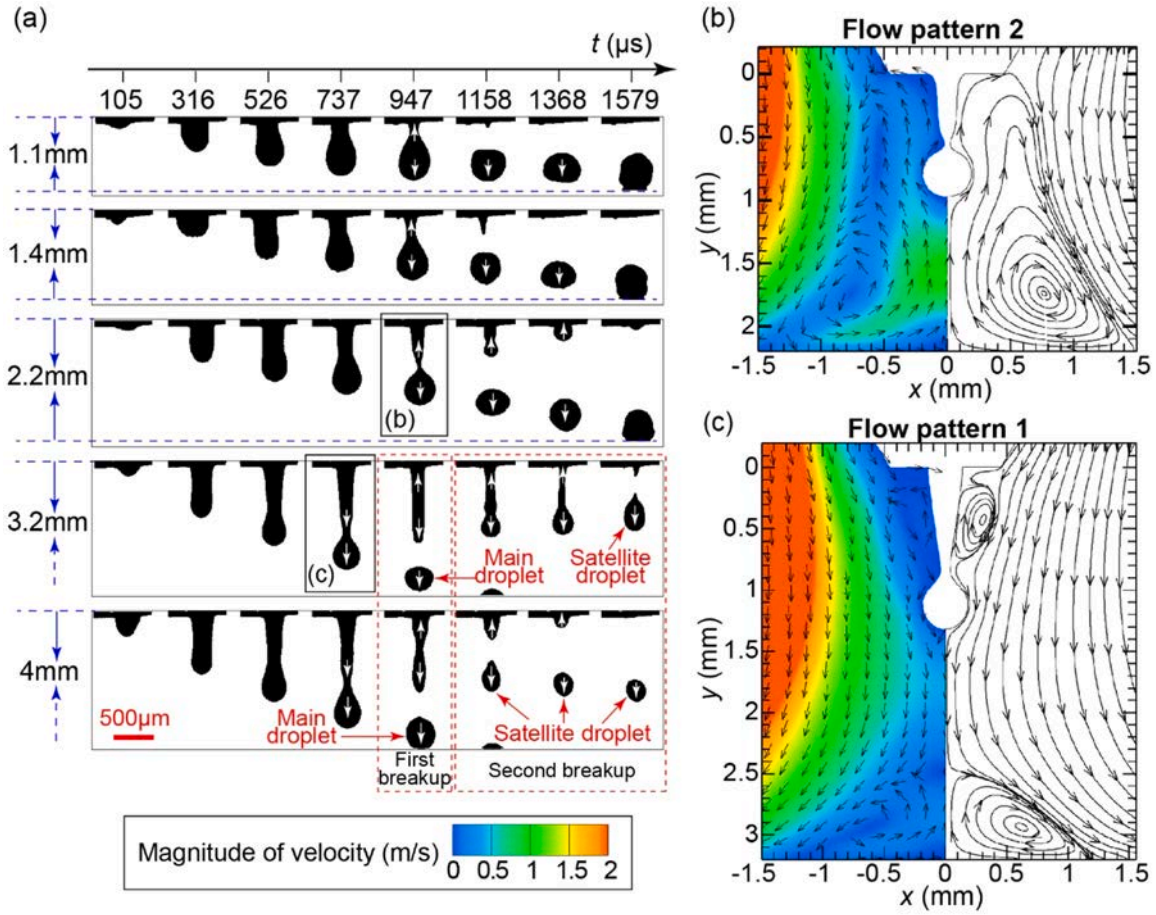

Fig. 11. (a) Binarized CCD snapshots of droplet formation at different deposition distances. Flow field simulation results of the typical flow patterns with droplet formation at different deposition distances: (b) H=2.2 mm; (c) H=3.2 mm. The shielding gas supply rate Q_{gas} is 3 L/min.

impinge on the substrate surface and form a stagnation circle, as shown in Fig. 9(b), eventually forming a large recirculation zone occupying the entire deposition space.

As depicted in Fig. 10, a smoke-wire was placed at 0.8 mm close to the substrate surface for capturing the practical airflow trace. The airflow smoke morphology at different deposition distances could verify the transition behavior of two airflow patterns. When H is relatively large (3.9 mm in Figs. 10(a), and 3.1 mm in Fig. 10(b)), the smoke is mainly distributed below the smoke-wire because the shielding gas flows downward with flow pattern 1 near the substrate. When H is small (2.2 mm in Figs. 10(c), and 1.5 mm in Fig. 10(d)), the smoke fills the entire deposition space since the shielding gas flows reverse with flow pattern 2 near the substrate. The results show that the transition of two airflow patterns occurs at the deposition distance between 2.2 mm~3.1 mm, which agrees well with the simulation result.

3.2. Effects of deposition distance on droplet formation

The pulse amplitude and width of the ejection signal were set to 3.7 V and 347 μs, respectively, to guarantee a stable breakup of the metal jet. In addition, the crucible was heated to 623 K to ensure the melting of the tin alloy, while the shielding gas supply rate was kept constant at 1.2 L/min to 3 L/min.

In a closed low-oxygen protection environment, such as an inert gas glove box, the droplet formation process is independent of the deposition distance. However, from the binarized CCD snapshots shown in Fig. 11(a), the droplet ejection behavior is significantly influenced by the dynamic shielding gas in the opening low-oxygen environment. The difference in the droplet formation process at different deposition distances is caused by the transition between two flow patterns. Fig. 11 (b) and (c) show the simulation results of two typical flow patterns with droplet formation. When H is less than 2.2 mm, the metal jet is shorter than the axial length of the recirculation zone and is sheared by shielding gas in the opposite direction. The jet then breaks up into a single droplet. However, for H over 3.2 mm, the jet becomes longer than the axial length of the recirculation zone, resulting in the jet root and tip being sheared by airflow in different directions. After the main droplet forms, the jet is susceptible to a secondary breakup with the formation of a satellite droplet. The flight velocity and diameter of the satellite droplet are highly stochastic and generally smaller than those of the main droplet, and its flight trajectory is precarious.

From Eqs. (6) and (7), the initial velocity of droplets and the break length of jets change with the ambient pressure at the nozzle outlet (P_a) and the average velocity of shielding gas ($\overline{v_g}$). P_a could be get by simulation directly. $\overline{v_g}$ could be obtained by calculating the average value of the airflow velocity on the central axis. However, it is inappropriate to take the average airflow velocity along the entire central axis as $\overline{v_g}$ when the deposition distance is greater than the jet length, since the shielding gas has a dynamic effect only in the metal jet vicinity. This study uses the normal jet break length when the metal jet is least affected by airflow, l_{norm}, as a reference. When the deposition distance is greater than the jet length, $\overline{v_g}$ is obtained by calculating the average airflow velocity from coordinates (0, 0) to (0, l_{jet}). That is

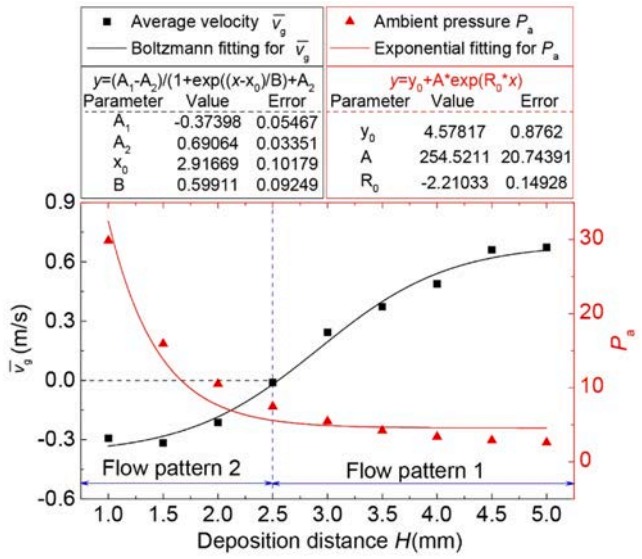

Fig. 12. Dependence of the airflow average velocity $\overline{v_g}$ and the ambient pressure P_a on the deposition distance H in simulation. The shielding gas supply rate Q_{gas}=3 L/min.

$$\overline{v_g} = \begin{cases} \dfrac{\int_0^{l_{norm}} v_g(y)dy}{l_{norm}} & H \geq l_{norm} \\ \dfrac{\int_0^{H} v_g(y)dy}{H} & H < l_{norm} \end{cases} \quad (8)$$

where l_{norm} is equal to 1.23 mm according to the experimental result in Fig. 6. $\overline{v_g} > 0$ means that the metal jet is mainly acted by the positive airflow force, while $\overline{v_g} < 0$ represents the reverse airflow force. The dependence of $\overline{v_g}$ and P_a on H in the simulation is shown in Fig. 12. When H is less than 2.5 mm, shielding gas flows backward with flow pattern 2. $\overline{v_g}$ increases in the negative direction. Meanwhile, P_a has a significant growth with the compression of airflow space. As H increases beyond 2.5 mm, shielding gas transforms from flow pattern 2 to flow pattern 1. $\overline{v_g}$ increases remarkably in the positive direction due to the decrease in the axial length of the recirculation zone. P_a decreases with the opening of airflow space and remains at a low level below 8 Pa.

From Fig. 12, as H increases, $\overline{v_g}$ gradually increases while P_a decreases. From Eqs. (5), (6), and (7), an increase in the shielding gas velocity and a decrease in the ambient pressure lead to a rise in the initial velocity of droplets and the break length of jets. To further investigate the airflow effect on droplet formation at different deposition distances. Two dimensionless numbers, the ratio of jet breaking length L_b and the ratio of droplet velocity V_d, were defined by taking the normal jet break length of 1.23 mm and the droplet initial velocity of 0.8 m/s (when the shielding gas supply rate is at a low level of 1.2 L/min) as ratio values, i.e., $L_b=l_b/1.23$ and $V_d=v_d/0.8$. $L_b>1$ indicates jet stretching, while $L_b<1$ denotes jet shortening. $V_d>1$ represents droplet accelerating, while $V_d<1$ implies droplet decelerating.

In the experiment, the dependence of L_b and V_d on the deposition distance H is shown in Fig. 13 (a) and (b). With 2.5 mm as a critical deposition distance, droplet ejection behavior is well-matched with the shielding gas flow patterns. When H is less than 2.5 mm, under the shielding gas backflow and the high ambient pressure, jet shortening and droplet deceleration with varying degrees are observed in airflow pattern 2. When H is larger than 2.5 mm, jet stretching and droplet acceleration occur in airflow pattern 1 under the strong positive airflow effect. Moreover, the hydrodynamic model developed in Section 2.3 demonstrates a consistent variation with the experiment. The NRMSE, for the ratio of metal jet breaking length is 0.34%, while for the ratio of droplet velocity is 1.45%. The current model is sufficient to explain the variations in jet breakup behavior at different deposition distances.

In addition, if the metal jet is excessively stretched by shielding gas ($L_b \geq 1.19$), the remaining jet is fragile to a secondary breakup. In a practical printing process, the deposition distance should be controlled below 2.8 mm to avoid satellite droplets affecting the fabrication quality.

The visual presentation for droplet formation at different deposition distances could be obtained in Supplementary Video 2.

3.3. Metal jet deflection in annular impinging jet shielding gas

Previous studies [43] have shown that nozzle processing defects may induce uneven wetting between the metal jet and the nozzle, further leading to the deflection of the droplet flight trajectory. Besides, the droplet deposition accuracy would decrease significantly as the deposition distance increases. However, in this study, the metal jet ejection behavior in the annular impinging jet shielding gas (Fig. 14 (a) and (b)) illustrates that the smaller the deposition distance, the more severe the metal jet deflection. The metal jet deflection at small deposition distances would decrease the printing accuracy, which differs from the droplet printing law in a closed low-oxygen environment. This indicates

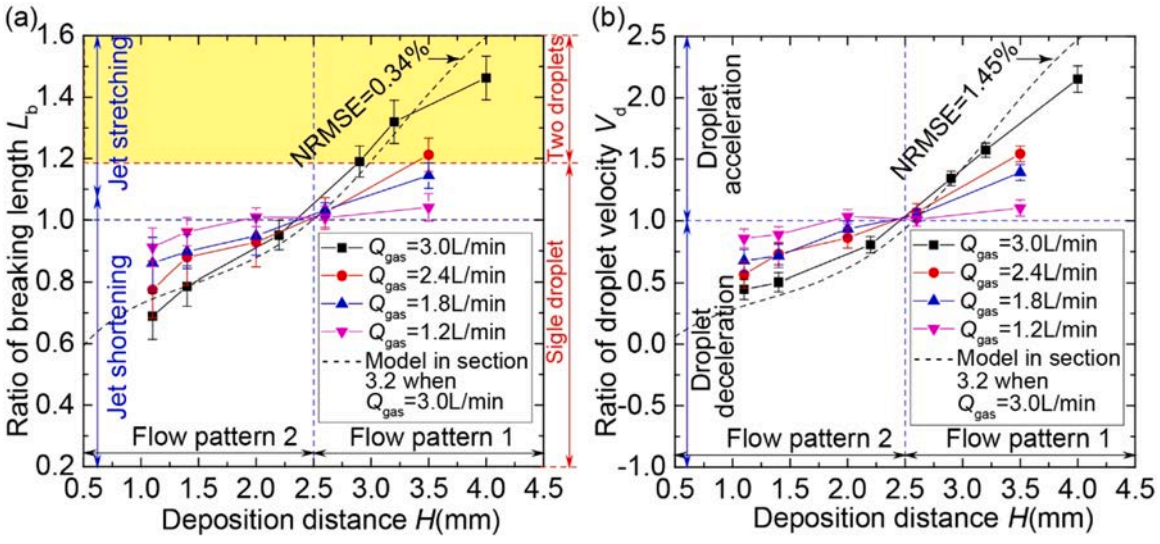

Fig. 13. Dependence of jet breaking length (a) and droplet velocity (b) on deposition distance in the experiment.

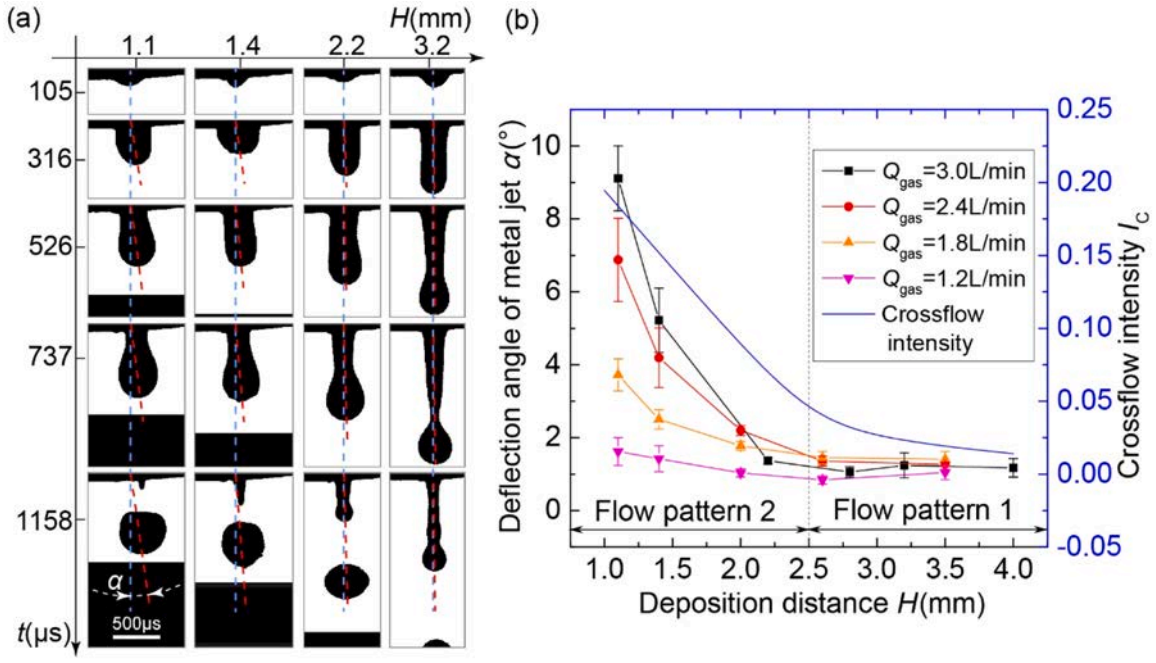

Fig. 14. (a) Binarized CCD Snapshots of the metal jet deflection behavior for Q_{gas}=3 L/min, and (b) metal jet deflection angle and crossflow intensity under different shielding gas supply rates. The blue dotted line in the figure is the nozzle central axis.

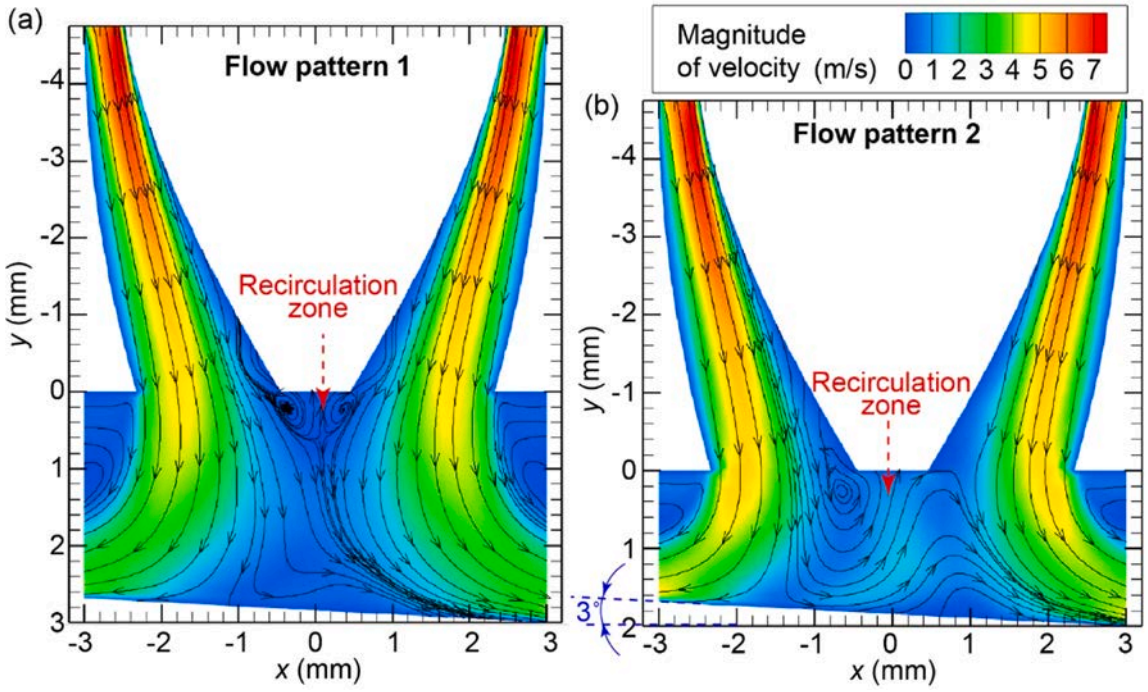

Fig. 15. Simulation results of the normal-section flow field for the shielding gas of (a) flow pattern 1 (H=3 mm) and (b) flow pattern 2 (H=2 mm). The substrate has a slight inclination angle of 3° to the nozzle surface. The shielding gas supply rate Q_{gas}=3 L/min.

that the metal jet deflection in the annular impinging jet shielding gas is caused by the printing substrate. The proximity of the substrate to the nozzle enhances the lateral force from the airflow on the metal jet.

The visual presentation for metal jet deflection at different deposition distances is shown in Supplementary Video 3.

The position of the printing substrate determines the deposition distance and printing angle of droplets. Ideally, the substrate is considered to be horizontal to the nozzle surface. However, in practical experiments, uncontrollable factors, such as the tolerance of machining and assembly in the substrate and nozzle, might cause the nozzle surface and the substrate surface to be slightly inclined instead of perfectly parallel. In a closed low-oxygen protective environment, this inclination does not affect the trajectory of metal jets at different deposition distances. However, in an opening shielding gas environment, such inclination could change the axisymmetric distribution property of shielding gas and cause the metal jet trajectory to deviate from the ideal case.

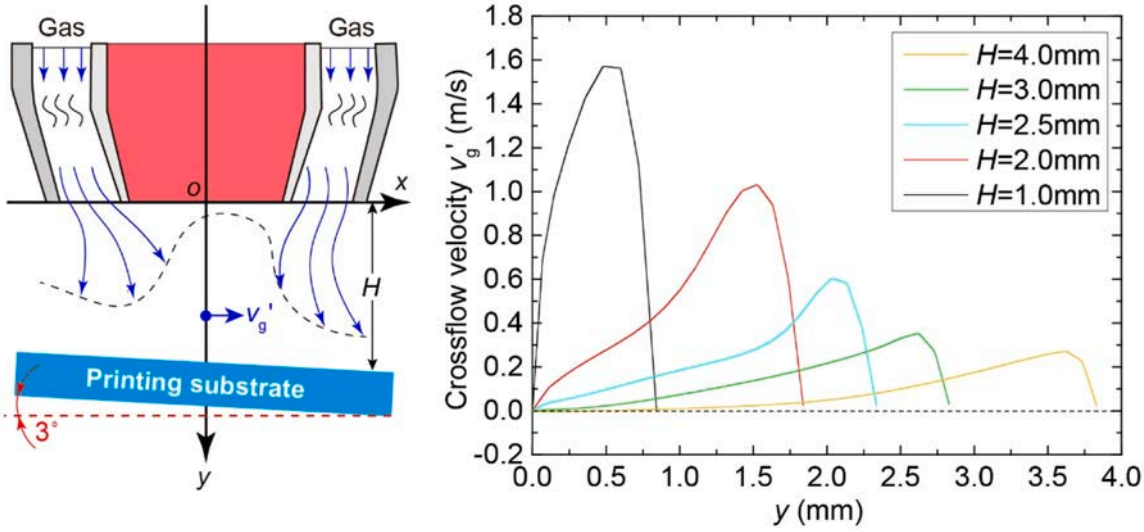

Fig. 16. Simulation results of crossflow velocity along the nozzle axis at different deposition distances. The shielding gas supply rate Q_{gas}=3 L/min.

Therefore, it is considered that the metal jet deflection is closely related to the assembly tolerance between the substrate and the nozzle.

To fully consider the effect of assembly tolerances on airflow distribution, a 3° slight inclination angle of the substrate surface to the nozzle surface was set in the shielding gas flow simulation. At the same time, a three-dimensional computational domain was used to investigate the airflow distribution in the case of substrate inclination. Fig. 15 (a) and (b) show the simulation results of the normal-section flow field for the shielding gas in flow pattern 1 (H=3 mm) and flow pattern 2 (H=2 mm), respectively. The slight inclination of the substrate does not affect the transition between the two airflow patterns, but results in a strong crossflow from shielding gas.

The simulation results of the crossflow velocity v_g' along the nozzle axis at different deposition distances are shown in Fig. 16. When the deposition distance is far away (e.g., H=4 mm), the substrate effect on the shielding gas at the nozzle outlet is weak, and the crossflow mainly distributes close to the substrate, so that a small peak value of v_g' occurs nearby the substrate surface. As H decreases, the substrate effect on the shielding gas at the nozzle outlet becomes stronger, increasing the peak value of v_g', and making the crossflow close to the nozzle exit. Eventually, a large deformation recirculation zone forms.

The crossflow is the main factor in generating the lateral force on the metal jet. Here, the dimensionless number I_C is used to scale the crossflow intensity, which is equal to the ratio of the average crossflow velocity in the central axis to the shielding gas supply rate ($\int_0^H v_g'(y)dy/(HQ_{gas})$). From the statistical analysis of metal jet deflection angle and crossflow intensity (Fig. 14(b)), metal jets affected by the strong crossflow in flow pattern 2 are deflected at different angles for $H\leq$2.5 mm. Note that the large error bar at a small deposition distance is caused by the randomness of the jet deflection angle rather than a measurement error, indicating a high randomness in the jet deflection angle attributed to the strong and random airflow disturbance. As the deposition distance declines, the metal jet deflection becomes more and more significant. On the contrary, due to the relatively weak crossflow in flow pattern 1 for H>2.5 mm, the deflection angle of metal jets can be controlled below 1.5°. Therefore, a minor deposition distance should be avoided to prevent metal jets from being excessively deflected by the crossflow.

Furthermore, it can be seen from Fig. 13 and Fig. 14 that the variations in metal jet breaking length, droplet velocity, and metal jet deflection angle with deposition distance are consistent under different shielding gas supply rates. The airflow disturbance on the droplet ejection could be weakened by reducing the airflow velocity. Although reducing the shielding gas supply rate benefits droplet ejection stability, it would sacrifice low-oxygen protective performance and increase the risk of droplet oxidation.

3.4. Droplet printing verification in an opening environment

3.4.1. Droplet deposition in annular impinging jet shielding gas

When a droplet impacts the substrate, the droplet keeps alternate spreading and recoiling to balance the kinetic and surface energy. The oscillation would stop when the kinetic energy is completely dissipated or the droplet solidifies [44]. Fig. 17 shows the typical moments of the metal droplet deposition process at different deposition distances. After several processes, such as impaction, spreading, recoil, and oscillation on the substrate, the droplet finally solidifies and forms a single hemispherical bump. There are significant differences in the droplet deposition behavior at different deposition distances. When the substrate is closed to the nozzle, the up-and-down oscillation of the droplets is less visible, while the final droplet deposition position deviates from the nozzle axis because of the shielding gas crossflow effect. As the deposition distance H increases, the spreading, recoiling, and oscillation of droplets become more and more obvious, at the same time the droplet deposition position is getting closer to the central axis due to the weakening crossflow. When H is greater than 2.8 mm, the spreading, recoiling, and oscillation of droplets are drastic, accompanied by the formation and deposition of satellite droplets. At the same time, the randomized falling trajectory of the satellite droplet may cause it to overlap or remelt with the main droplet, further making the droplet deposition morphology unpredictable.

The visual presentation of the metal droplet deposition process at different deposition distances is shown in Supplementary Video 4.

Variations in droplet deposition behavior could be characterized by the maximum spreading factor (β) and the maximum dimensionless height (γ), where β is defined as the ratio of the maximum droplet spreading diameter to the initial droplet diameter ($w_{d,max}/d_d$), and γ is the ratio of the maximum droplet recoiling height to the initial droplet diameter ($h_{d,max}/d_d$). The relationship between β and numerous impact parameters is usually based on the balance between inertial, viscous, and capillary to establish the physical model. Clanet et al. [45] summarized a scaling law, $\beta \propto We^{1/4}$, according to a mass conservation argument, where We is the Weber number defined with the droplet properties as $We = \rho_m d_d v_d^2/\mu_m$.This means that the maximum spreading rate is positively correlated with the droplet impact velocity. Although there is no well-established study to characterize γ quantitatively, Mao

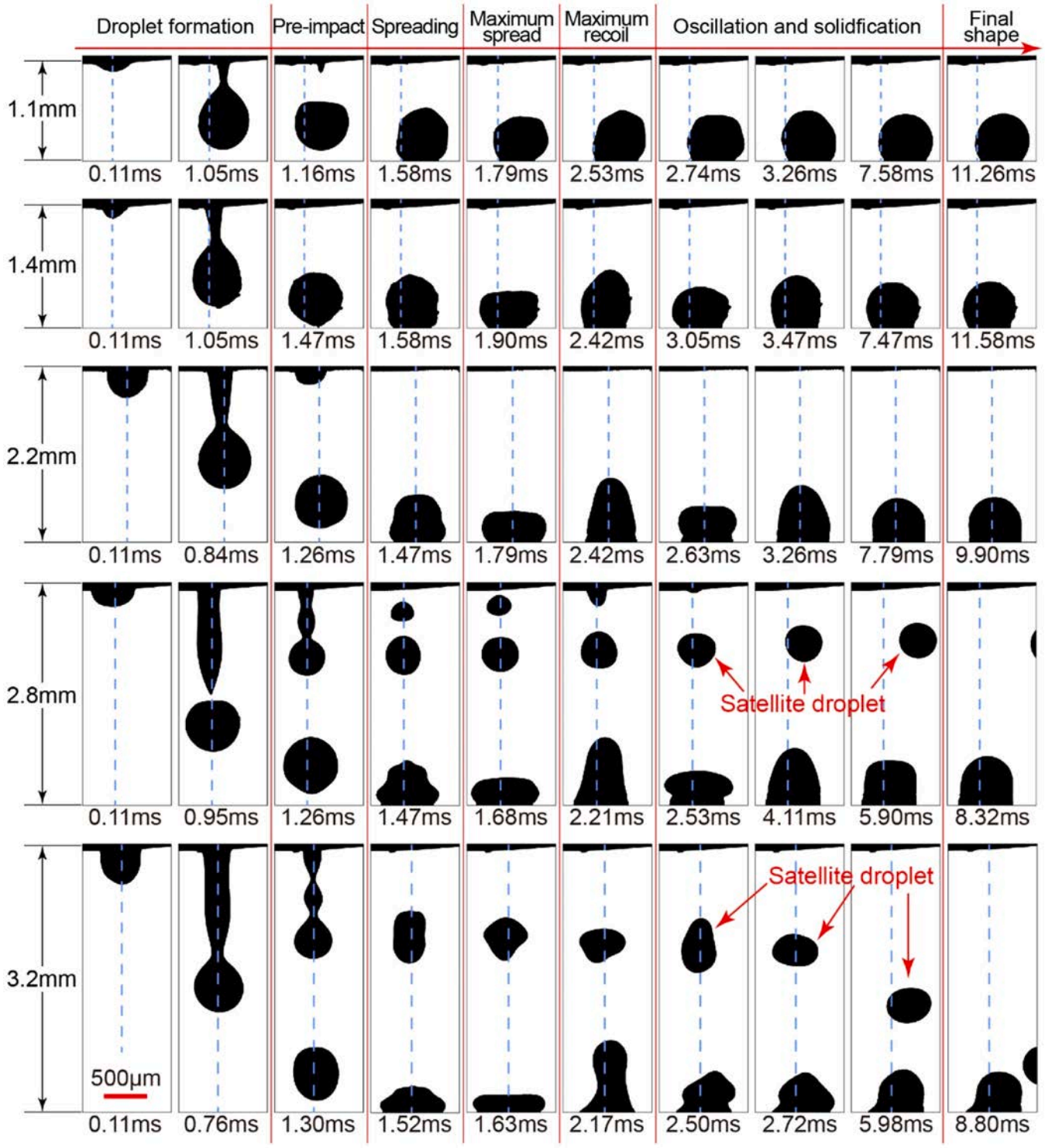

Fig. 17. Binarized CCD Snapshots of the metal droplet deposition behavior for Q_{gas}=3 L/min. The blue dotted line in the figure is the nozzle's central axis.

et al. [46] investigated the droplet recoiling process experimentally and theoretically, showing that a larger droplet impact velocity would lead to higher droplet rebound height, which may even cause droplet breakup and separation during its recoiling.

Fig. 18 shows the dependence of the droplet maximum spreading factor, maximum dimensionless height, and impact velocity on the deposition distance in this study. The droplet impact velocity grows with the increasing deposition distance and the shielding gas flow pattern transition, which further contributes to the larger spreading rate and recoiling height. When H is 1.1 mm, β and the γ are both close to 1, indicating that neither the spreading nor the recoil is significant, while the shielding gas crossflow makes the droplet slightly jittery before it completes solidification, as shown by the snapshots between 2.53 and 7.58 ms in Fig. 17. When H is 3.2 mm, γ up to 1.38, there is even a tendency for the liquid surface to break up at the maximum recoil height due to the intense droplet recoil. The unstable liquid surface eventually leads to an irregular droplet solidification morphology, as shown by snapshots between 2.17 and 8.80 ms in Fig. 17. When H is 2.2 mm, near

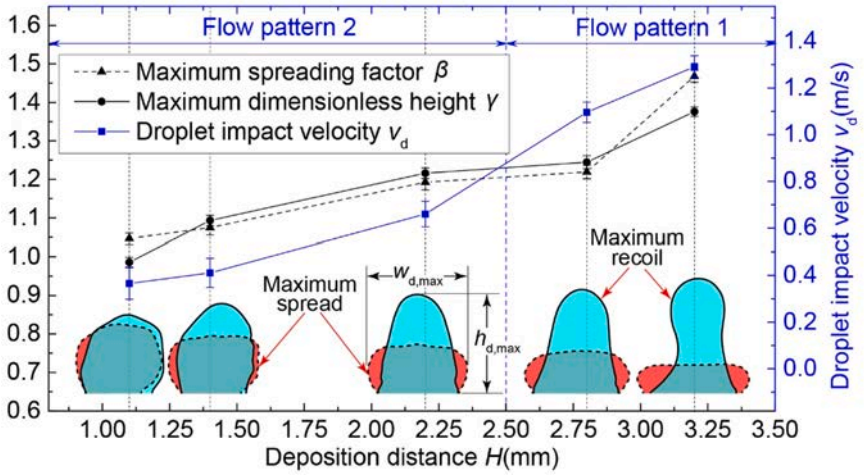

Fig. 18. Dependence of the droplet maximum spreading factor, maximum dimensionless height, and impact velocity on the deposition distance. The shielding gas supply rate Q_{gas}=3 L/min.

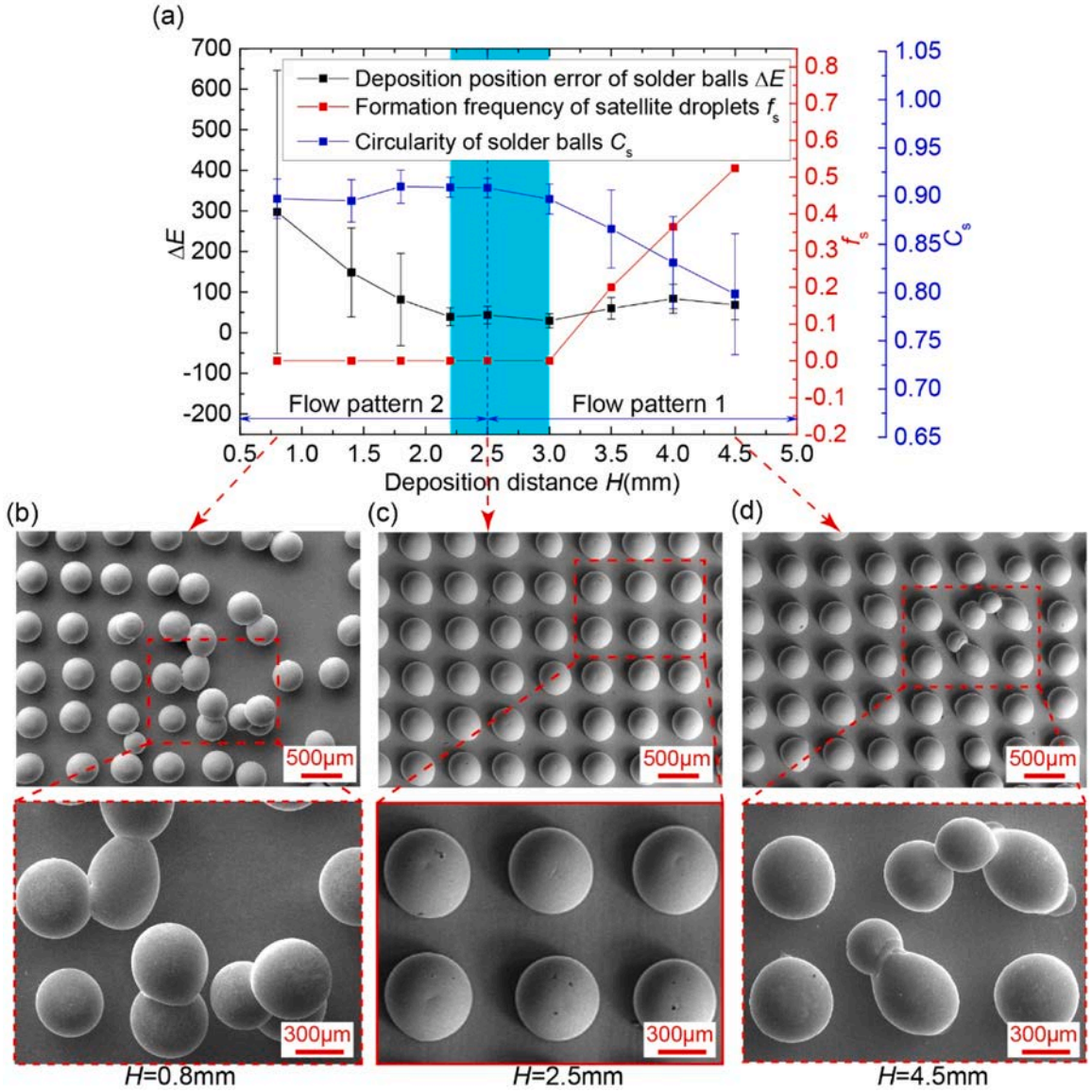

Fig. 19. (a) Deposition position error of solder balls, formation frequency of satellite droplets, and circularity of solder balls in 15×15 solder ball arrays printing. SEM images of the solder ball arrays with (b) H=0.8 mm, (c) H=2.5 mm, and (d) H=4.5 mm, respectively.

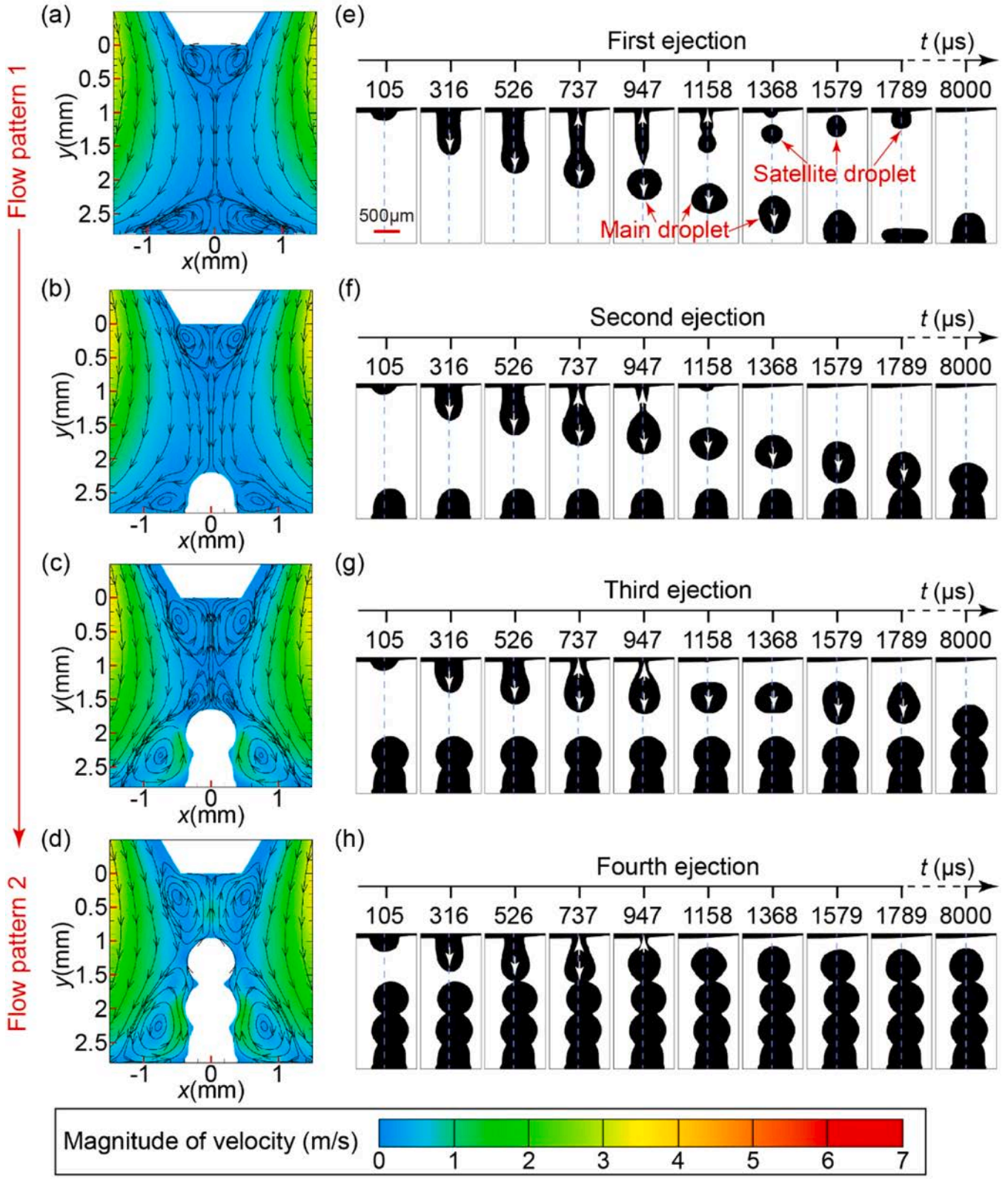

Fig. 20. Shielding gas flow field distribution before (a) first droplet ejection, (b) second droplet ejection, (c) third droplet ejection, and (d) fourth droplet ejection. (e) ~(h) CCD Snapshots of four sequential droplet ejections. The shielding gas supply rate Q_{gas}=2.7 L/min, while the distance between the substrate and nozzle is kept at 2.8 mm.

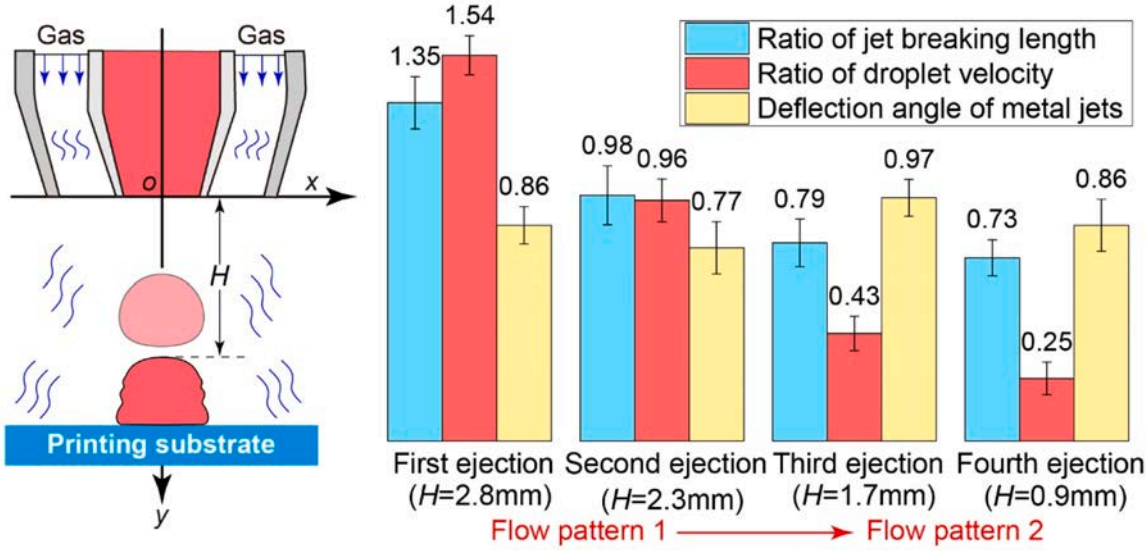

Fig. 21. Ratio of jet breaking length, ratio of droplet velocity, and deflection angle of metal jets during droplet pileup. The shielding gas supply rate Q_{gas}=2.7 L/min, while the distance between the substrate and nozzle is kept at 2.8 mm.

the two airflow patterns transition, the droplet is capable of accurate printing at the nozzle axis after a normal oscillation due to the moderate droplet impact velocity and weakened crossflow.

To obtain stable ejection and accurate printing parameters for metal droplets in the annular impinging jet shielding gas, 15×15 solder ball arrays were printed at different deposition distances ranging from 0.8 mm to 4.5 mm. During the printing process, the shielding gas supply rate increased linearly from 1.5 L/min to 3 L/min. Besides, gold-clad plates were chosen as the printing substrate, and the printing pitch of the solder balls was set to 0.8 mm.

The deposition position error of solder balls, ΔE, the formation frequency of satellite droplets, f_s, and the circularity of solder balls, C_s, at different deposition distances, are shown in Fig. 19(a). f_s is the ratio of the count of satellite droplets to that of ejections. C_s is derived from the relation between the solder ball shape area, A_{ball}, and the solder ball shape perimeter, P_{ball}. The circularity measure is defined as [47]

$$C_s = \frac{4\pi A_{ball}}{{P_{ball}}^2} \tag{9}$$

Statistics show that when H is less than 2.2 mm, solder balls are capable of reaching a high circularity of ~0.9. However, affected by the shielding gas crossflow, the printing accuracy of droplets is poor and the deposition position is highly random. As demonstrated in the SEM image of the solder ball array for H=0.8 mm in Fig. 19(b), droplet deposition positions are far from ideal, where chaotic overlapping of solder balls is observed. For H above 3.2 mm, droplets could be deposited accurately, while the formation frequency of satellite droplets is relatively high. The remelting of smaller satellite droplets with main droplets leads to irregular printing shapes and even short circuits in adjacent balls, which reduces the circularity of solder balls, as shown in Fig. 19(d). When H is around 2.5 mm, which is the transition region between the two airflow patterns, both the airflow velocity and the ambient pressure are relatively low (Fig. 12). This condition allows high-precision and ideal-circularity printing for solder balls without satellite droplet formation, as reflected in Fig. 19(c).

Accordingly, the deposition distance should be near the transition region of two airflow patterns to achieve stable ejection and accurate printing, as illustrated by the blue region in Fig. 19(a), which diminishes the airflow disturbance on the droplet ejection to a low level.

3.4.2. *Metal droplet ejection process during its pileup*

During the 3D forming based on metal droplet ejection, the nozzle would be far from the substrate but close to the current printing layer as droplets pile up layer by layer. The printed region of the part may affect the airflow pattern, changing the metal droplet ejection behavior. Since a single droplet is a basic unit for forming 3D parts, in order to clarify the influence of the printed region on the droplet ejection behavior during 3D printing, the airflow field transition and the droplet formation process during the single droplet pileup were investigated by simulation and experiment. Fig. 20 (a)~(d) show the shielding gas flow field distribution before each droplet ejection, while Fig. 20 (e)~(h) illustrate the CCD snapshots of four sequential droplet ejections. The distance between the substrate and the nozzle is kept at 2.8 mm during the droplet pileup. It can be seen that the droplet pileup increases the airflow recirculation range, leading to a transition from shielding gas flow pattern 1 to flow pattern 2, which is similar to the airflow pattern transition caused by the proximity between the substrate and the nozzle in Fig. 9. The droplet pileup could prevent the annular airflow from converging on the axis. For the first ejection, the satellite droplet would be formed by the secondary breakup of the metal jet in airflow pattern 1 (as shown in Fig. 20(e)). However, since the droplet pileup would reduce the deposition distance and change the airflow pattern, the metal jet breaking length is gradually reduced during the second to fourth ejections, with the secondary breakup disappearing (as shown in Fig. 20 (f)~(h)).

The visual presentation for the metal droplet ejection process during its pileup could be found in Supplementary Video 5.

Fig. 21 statistics the ratio of jet breaking length, the ratio of droplet velocity, and the deflection angle of metal jets during droplet pileup. As droplets pile up and the airflow pattern changes, the jet breaking length and the droplet velocity gradually decrease. For the second ejection with a deposition distance of 2.3 mm, the ratio of jet breaking length and the ratio of droplet velocity are very close to 1, indicating that the second droplet ejection is less affected by airflow disturbance. In addition, unlike direct deposition on the substrate, there is no significant variation in the metal jet deflection angle as droplets pile up, although the deposition distance decreases. It is also evident in Fig. 20 that the metal jet trajectory is maintained in a good alignment with the blue central axis for each droplet ejection. This provides additional evidence that the jet deflection is dominated by the substrate. Although the deposition distance decreases during the droplet pileup, the jet angle is hardly affected due to the substrate being motionless.

In practical droplet printing, the metal jet trajectory is susceptible to the airflow field axisymmetry near the nozzle, which is highly

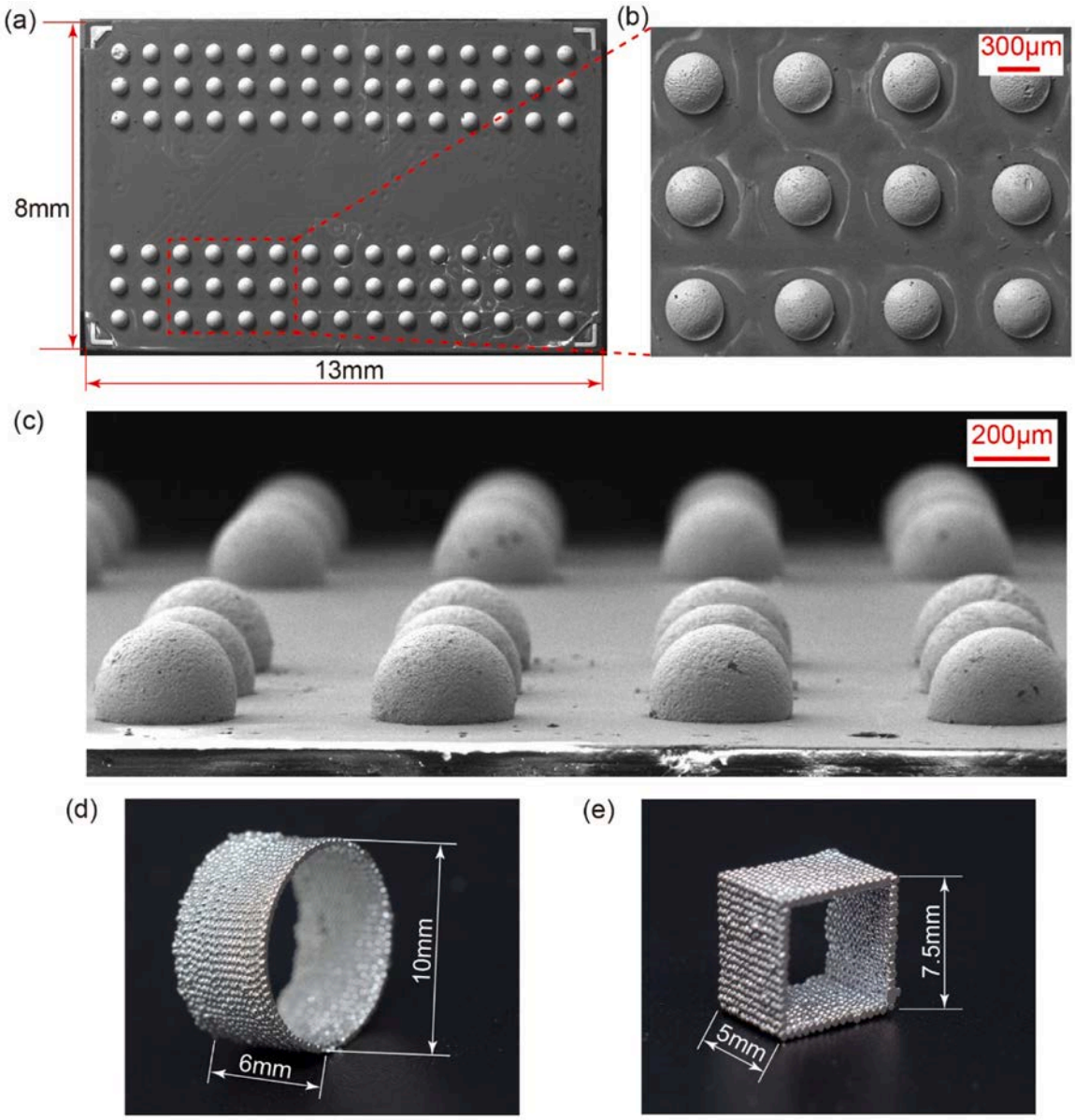

Fig. 22. (a) A memory chip with solder balls printed by metal droplets. (b) A close-up view of (a). (c) A SEM front view of (a). (d) A cylindrical and (e) a square thin-wall tube printed by metal droplets under shielding gas.

dependent on the morphology of the current printing layer. It is necessary to optimize the printing trajectory to avoid the airflow non-axisymmetric distribution, while the droplet deposition distance control is also an essential strategy to mitigate the airflow disturbance.

3.4.3. Processing and forming in an opening environment

Based on the above analysis, a ball grid array (BGA) chip ball-mounting was attempted to verify the research feasibility. Fig. 22(a) displays a memory chip with its solder balls printed by metal droplets in the annular impinging jet shielding gas at a deposition distance of 2.5 mm. Fig. 22(b) shows a partially magnified SEM image of the chip in Fig. 22(a). With an overall chip size of 13 mm×8 mm and a pad diameter of ~380 μm, metal droplets are precisely printed on pads. As presented in Fig. 22(c), the printed BGA solder balls feature uniformly rounded hemispherical morphologies without remelting or overlapping other satellite droplets. This indicates that controlling the deposition distance is an effective way to reduce the airflow disturbance on the droplet ejection in the annular impinging jet shielding gas. Furthermore, to verify the applicability of the study in the 3D structure building, a cylindrical and a square thin-wall tube were printed under a deposition distance of 2.5 mm, as shown in Fig. 22 (d) and (f). It can be seen that the droplets could be ejected and piled up as expected under the shielding gas environment, exhibiting a satisfactory 3D structure printing capability.

4. Conclusions

In this study, the effect mechanism of annular impinging jet shielding gas on metal droplet formation and metal jet deflection was first revealed. To investigate the droplet ejection process in shielding gas, an airflow simulation based on the RSM, an airflow smoke-wire observation, a hydrodynamic model construction, and a droplet ejection experiment were combined and applied. An innovative suppression strategy of airflow disturbance for metal droplet ejection was proposed by controlling the deposition distance in the annular impinging jet shielding gas. As the deposition distance reduces, the annular impinging jet shielding gas transforms from flow pattern 1 to flow pattern 2, further affecting droplet ejection behavior. The strong velocity difference at the

gas-liquid interface in flow pattern 1 would cause jet stretching and droplet acceleration, even forming satellite droplets when metal jets are overstretched. In contrast, the recirculation zone size and the ambient pressure increase significantly in flow pattern 2, leading to jet shortening and droplet deceleration. Besides, excessive proximity between the nozzle and the substrate could enhance shielding gas crossflow because of component assembly tolerances, causing metal jets to deflect. By adjusting the deposition distance to the transition region of two typical airflow patterns, the effect of shielding gas on droplet formation is minimized, allowing stable ejection and accurate printing of metal droplets. Finally, a BGA chip was accurately ball-mounted without satellite droplet overlapping in an opening printing environment, verifying the reliability of the airflow disturbance suppression strategy. Two thin-wall tubes were printed under the shielding gas, exhibiting the applicability of the research for practical structure printing. This study permits new insights into the effect mechanism of shielding gas-impinging behavior on metal droplet ejection. In addition, the theoretical guidance for the opening printing of metal droplets might promote the industrial application of metal droplet-based 3D printing technology in an intelligent, automated, and lightweight way.

CRediT authorship contribution statement

Lin Su: Investigation. **Jun Luo:** Writing – review & editing, Project administration, Funding acquisition. **Yi Zhou:** Writing – original draft, Validation, Software, Methodology, Investigation, Formal analysis, Data curation, Conceptualization. **Hongcheng Lian:** Writing – review & editing, Supervision, Project administration, Funding acquisition. **Lehua Qi:** Writing – review & editing, Supervision, Project administration, Methodology, Funding acquisition.

Declaration of Competing Interest

The authors declare that they have no known competing financial interests or personal relationships that could have appeared to influence the work reported in this paper.

Data availability

Data will be made available on request.

Acknowledgements

This work was supported by the National Natural Science Foundation of China (No. 52231004); the China Postdoctoral Science Foundation (2022M712592); and the JFJ comprehensive research project (KJ2021–82).

Appendix A

When applying a jet signal, the molten metal in the vibration chamber is forced forward by the vibration rod. Part of the metal fluid flows into the nozzle to form the metal jet, while the other part flows into the annular side gap. According to the fluid mechanic theory, when the vibration rod moves forward at velocity v_0, the total flow rate, Q, can be expressed as

$$Q = S_v v_0 \tag{A.1}$$

where $S_v = \pi {d_v}^2/4$ is the cross-sectional area of the vibration rod head.

The flow rate of molten metal through the nozzle, Q_N, is

$$Q_N = S_{n2} v_3 \tag{A.2}$$

where $S_{n2} = \pi {d_{n2}}^2/4$ is the cross-sectional area of the nozzle outlet; v_3 is the metal jet ejection velocity.

The flow rate in the annular side gap, Q_L, can be expressed as [48]

$$Q_L = \pi d_v \left(\frac{\delta^3}{12\mu_m h_v} \Delta P_L - \frac{\delta}{2} v_0 \right) \tag{A.3}$$

where ΔP_L is the pressure difference between the upper and lower ends of the annular lateral gap. The relationship between P_t and P_b is $P_t = P_b + \rho_m g h$. Thus, as the vibration rod moves forward, the pressure difference in the lateral gap, ΔP_L, can be expressed as

$$\Delta P_L = P - P_b - \rho_m g h \tag{A.4}$$

The total head loss of molten metal from the bottom surface of the vibration rod to the nozzle outlet is [49]

$$\Delta h = \frac{f_1 {v_1}^2 l_v}{2 g d_c} + \frac{{v_2}^2}{2g}\left(\frac{f_2 l_{n1}}{d_{n1}} + K_1 \right) + \frac{{v_3}^2 K_2}{2g} = \frac{P - P_{Lap}}{\rho_m g} + \left(l_v + l_{n1} + l_{n2} \right) \tag{A.5}$$

where f_1 and f_2 are the head loss coefficients along the straight flow channel sections at positions ① and ②, respectively, which are equal to $64/Re_L$ when the flow is laminar, and Re_L is the Reynolds number of metal jets; K_1 is the local head loss coefficient at the sudden contraction between ① and ②, calculated by $K_1 = 0.42(1 - {d_{n1}}^2/{d_c}^2)$; and K_2 is the local head loss coefficient at the gradual contraction between ② and ③, K_2=0.04 when the nozzle contraction angle θ is 45°; v_1 and v_2 are the fluid velocities at positions ① and ②, respectively, expressed by v_3 as $v_1 = {d_{n2}}^2 v_3/{d_c}^2$ and $v_2 = {d_{n2}}^2 v_3/{d_{n1}}^2$; P_{Lap} is the Laplace pressure generated by the capillary force at the nozzle outlet, calculated by $P_{Lap} = 2\sigma/d_{n2} + P_a$.

From the mass conservation equation $Q = Q_N + Q_L$ and Eqs. (A.1)~(A.5), the metal jet ejection velocity, v_3, can be calculated form the ambient pressure, P_a, as

$$v_3 = -\frac{B}{2A} + \frac{\sqrt{B^2 + 4AC - 4AP_a}}{2A} \tag{A.6}$$

Here, $A = 0.21\rho_m {d_{n2}}^4/{d_{n1}}^4(1 - {d_{n1}}^2/{d_c}^2) + 0.02\rho_m$, $B = 32\mu_m {d_{n2}}^2(l_v/{d_c}^4 + l_{n1}/{d_{n1}}^4) + 3\mu_m h_v {d_{n2}}^2/d_v\delta^3$, and $C = 3\mu_m h_v/\delta^3(d_v v_0 + 2v_0\delta) + \rho_m g(l_v + l_{n1} + l_{n2} + h) + P_b - 2\sigma/d_{n2}$.

Since the Froude number of metal jets $Fr = v_3/\sqrt{g d_{n2}} \approx 60 \gg 1$ and the Bond number $Bo = \rho_m g {d_{n2}}^2/\sigma \approx 0.011 \ll 1$, gravity is neglected compared to inertial force and surface tension. Driven by the vibration rod, the metal jet ejects from the nozzle at velocity v_3 and must overcome the nozzle capillary

tension to keep the jet growing. Then the jet starts to neck and break up under the combination of viscous tension, jet capillary tension, and shielding gas shear force, eventually forming a metal droplet with an initial velocity of v_d. During jet growing and necking, the jet tip velocity decreases from v_3 to v_d, and the jet radius at the necking position gradually decreases from $d_{n2}/2$ to 0. Assuming that the driving signal disappears at time t_1, the jet breaks up at time t_2, and the jet diameter is approximately equal to the diameter of the nozzle outlet at the moment $0\sim t_1$; meanwhile, the jet tip velocity at the moment $0\sim t_1$ and the jet cross-sectional area at the moment $t_1\sim t_2$ both change linearly. Then the jet length, l_{jet}, and the diameter at the jet necking, d_{jet}, could be obtained from $l_{jet}(t) = \int_0^t (v_3 + (v_d - v_3)t/t_2)dt$.

The initial velocity of the droplet, v_d, was obtained by establishing the momentum model of jet ejection [50]. During the time $0\sim t_1$ when the driving signal is applied, the mass flux of metal fluid through the nozzle is $\rho_m S_{n2} v_3$, and the total momentum of the metal jet can be expressed as

$$p_{total} = \rho_m S_{n2} {v_3}^2 t_1 \tag{A.7}$$

When the jet flows out, the capillary tension at the nozzle outlet, τ_σ, is approximated as $\tau_\sigma = -\pi d_{n2}\sigma/2$, then the momentum transferred by the nozzle capillary tension during jet growing, $p_{\sigma 1}$, is

$$p_{\sigma 1} = -\frac{1}{2}\pi d_{n2}\sigma t_1 \tag{A.8}$$

The momentum transferred by the jet capillary tension during jet necking, $p_{\sigma 2}$, is

$$p_{\sigma 2} = -\int_{t_1}^{t_2} \frac{1}{2}\pi\sigma d_{jet}(t)dt = -\frac{1}{3}d_{n2}\pi\sigma\left(t_2 - t_1\right) \tag{A.9}$$

In a slender jet, the viscous tension τ_μ mainly comes from the extensional viscosity ($3\mu_m$), which is given by

$$\tau_\mu = 3\mu_m A\partial_y v_3 \tag{A.10}$$

where A is the jet cross-sectional area, $\partial_y v_3$ is the jet stretching rate, and y is the axial coordinate.

Correlating the stretching rate, the change in cross-sectional area, and the continuity equation yields

$$\frac{D}{Dt}A = -A\partial_y v_3 \tag{A.11}$$

Integrating Eq. (A.11)at the moment $t_1\sim t_2$ gives

$$A(t_2) - A(t_1) = \int_{t_1}^{t_2} \frac{D}{Dt}A dt = \int_{t_1}^{t_2} -\frac{\tau_\mu}{3\mu_m}dt = -\frac{p_\mu}{3\mu_m} \tag{A.12}$$

Thus, as the jet cross-sectional area reduces from S_{n2} to 0, the momentum transferred by the viscous tension, p_μ, is

$$p_\mu = -3\mu_m S_{n2} \tag{A.13}$$

During droplet formation, shielding gas exerts an interfacial shear force on metal jets, as shown in Fig. 7(b). The interfacial shear force of shielding gas on metal jets, τ_s, is mainly affected by the average velocity of shielding gas, $\overline{v_g}$ [51]. According to Sidi-Ali at all [52], τ_s can be expressed as

$$\tau_s = \frac{f_s \rho_g \overline{v_g}|\overline{v_g}|}{2} \tag{A.14}$$

where the shear factor f_s is given by $f_s = c_1 {Re_g}^{c_2}$. Re_g is the Reynolds number of shielding gas, and c_1, c_2 are the empirical constants. If the variation of the jet radius in metal jet evolution is neglected, the momentum transferred by the airflow shear force, p_s, can be approximated as

$$p_s \approx \tau_s \pi d_{n2}\int_0^{t_2} l_{jet}(t)dt = \tau_s \pi d_{n2}\left(\frac{v_d}{6} + \frac{v_3}{3}\right){t_2}^2 \tag{A.15}$$

Assuming that the residual jet velocity after the jet breakup is zero, the total momentum of the system is equal to the initial momentum of the droplet, p_d, i.e.

$$p_d = \frac{1}{6}\pi {d_d}^3 \rho_m v_d \tag{A.16}$$

From the theory of momentum conservation, inferring

$$p_d = p_{total} + p_{\sigma 1} + p_{\sigma 2} + p_\mu + p_s \tag{A.17}$$

From Eqs. (A.7)~(A.9), (A.13) and (A.15)~(A.17), v_d could be expressed as

$$v_d = \frac{D{v_3}^2 + Ev_3\overline{v_g}|\overline{v_g}| - F}{G - H\overline{v_g}|\overline{v_g}|} \tag{A.18}$$

Here, $D = 3\rho_m {d_{n2}}^2 t_1$, $E = 2f_s\rho_g d_{n2}{t_2}^2$, $F = 9{\mu_m}{d_{n2}}^2 + 2d_{n2}\sigma t_1 + 4d_{n2}\sigma t_2$, $G = 2{d_d}^3\rho_m$, and $H = f_s\rho_g d_{n2}{t_2}^2$.

The jet break length at time t_2 is expressed as

$$l_b = \int_0^{t_2}\left(v_3 + \frac{v_d - v_3}{t_2}t\right)dt = \frac{1}{2}\left(v_3 + v_d\right)t_2 \tag{A.19}$$

References

[1] T.Y. Ansell, Current status of liquid metal printing, J. Manuf. Mater. Process. 5 (2021) 31.
[2] L. Qi, Y. Chao, J. Luo, J. Zhou, X. Hou, H. Li, A novel selection method of scanning step for fabricating metal components based on micro-droplet deposition manufacture, Int. J. Mach. Tools Manuf. 56 (2012) 50–58.
[3] F. Torrisi, T. Hasan, W. Wu, Z. Sun, A. Lombardo, T.S. Kulmala, G.W. Hsieh, S. Jung, F. Bonaccorso, P.J. Paul, D. Chu, A.C. Ferrari, Inkjet-printed graphene electronics, ACS Nano 6 (2012) 2992–3006.
[4] E. Govekar, A. Jeromen, A. Kuznetsov, M. Kotar, M. Kondo, Annular laser beam based direct metal deposition, Procedia CRIP 74 (2018) 222–227.
[5] Z. Sun, W. Guo, L. Li, Numerical modelling of heat transfer, mass transport and microstructure formation in a high deposition rate laser directed energy deposition process, Addit. Manuf. 33 (2020) 101175.
[6] Y. Kara, N.K. Kovács, P. Nagy-György, R. Boros, K. Molnár, A novel method and printhead for 3D printing combined nano-/microfiber solid structures, Addit. Manuf. 61 (2023) 103315.
[7] A. Hatem, C. Schulz, T. Schlaefer, J.T. Boobhun, N. Stanford, C. Hall, Influence of laser absorption by water- and gas-atomised powder feedstock on Laser metal deposition of AISI 431 stainless steel, Addit. Manuf. 47 (2021) 102242.
[8] M. Fang, S. Chandra, C.B. Park, Building three-dimensional objects by deposition of molten metal droplets, Rapid Prototyp. J. 14 (2008) 44–52.
[9] Y. Yokoyama, K. Endo, T. Iwasaki, H. Fukumoto, Variable-size solder droplets by a molten-solder ejection method, J. Micro Syst. 18 (2009) 316–321.
[10] T. Metz, W. Streule, R. Zengerle, P. Koltay, StarTube: a tube with reduced contact line for minimized gas bubble resistance, Langmuir 24 (2008) 9204–9206.
[11] Z. Shu, M. Fechtig, F. Lombeck, M. Breitwieser, R. Zengerle, P. Koltay, Direct drop-on-demand printing of molten solder bumps on enig finishing at ambient conditions through starjet technology, IEEE Access 8 (2020) 210225–210233.
[12] V.A. Beck, N.N. Watkins, A.S. Ashby, A.A. Martin, P.H. Paul, J.R. Jeffries, A. J. Pascall, A combined numerical and experimental study to elucidate primary breakup dynamics in liquid metal droplet-on-demand printing, Phys. Fluids 32 (2020) 112020.
[13] M. Zenou, A. Sa'ar, Z. Kotler, Laser transfer of metals and metal alloys for digital microfabrication of 3D objects, Small 11 (2015) 4082–4089.
[14] M. Liu, H. Yi, H. Cao, R. Huang, L. Jia, Heat accumulation effect in metal droplet-based 3D printing: evolution mechanism and elimination Strategy, Addit. Manuf. 48 (2021) 102413.
[15] H. Merrow, J.D. Beroz, K. Zhang, U.P. Muecke, A.J. Hart, Digital metal printing by electrohydrodynamic ejection and in-flight melting of microparticles, Addit. Manuf. 37 (2021) 101703.
[16] J. Luo, R. Pohl, L. Qi, G.-W. Römer, C. Sun, D. Lohse, C.W. Visser, Printing functional 3D microdevices by laser-induced forward transfer, Small 13 (2017) 1602553.
[17] S.L. Li, Z.Y. Wei, D. Jun, G.X. Zhao, X. Wang, B.H. Lu, Research on the manufacturing of electrical power fittings based on metal droplet deposition, Appl. Phys. A: Mater. Sci. Process. 123 (2017) 1–7.
[18] Y. Chao, A novel selection method of slice thickness in metal micro-droplet deposition manufacture, J. Manuf. Process. 21 (2016) 153–159.
[19] M. Meda, P. Mehta, C. Mahajan, B. Kahn, D. Cormier, Magnetohydrodynamic liquid metal droplet jetting of highly conductive electronic traces, Flex. Print. Electron. 6 (2021) 035002.
[20] D. Lu, F.M. Xu, L. Zhao, Y.F. Fu, W. Dong, Y. Tan, A. Kawasaki, Fabrication of BGA solder balls by pulsated orifice ejection method, 14th. IEEE Int. Conf. Electron. Packag. Technol., 2013, pp. 694–697, 14th.
[21] J. Luo, L. Qi, S. Zhong, J. Zhou, H. Li, Printing solder droplets for micro devices packages using pneumatic drop-on-demand (DOD) technique, J. Mater. Process. Technol. 212 (2012) 2066–2073.
[22] A. Amirzadeh, M. Raessi, S. Chandra, Producing molten metal droplets smaller than the nozzle diameter using a pneumatic drop-on-demand generator, Exp. Therm. Fluid. Sci. 47 (2013) 26–33.
[23] fish 0,punct]">Y. Zhou, L.H. Qi, J. Luo, S. Lin, Investigation on the effect mechanism of micro-domain shielding gas on metal droplet ejection process, J. Mech. Eng. 59 (2023) 219–230 (In Chinese).
[24] E.M. Moore, R.L. Shambaugh, D.V. Papavassiliou, Analysis of isothermal annular jets: Comparison of computational fluid dynamics and experimental data, J. Appl. Polym. Sci. 94 (2004) 909–922.
[25] A. Nasr, J. Lai, Comparison of flow characteristics in the near field of two parallel plane jets and an offset plane jet, Phys. Fluids 9 (1997) 2919–2931.
[26] M. Fénot, E. Dorignac, R. Lantier, Heat transfer and flow structure of a hot annular impinging jet, Int. J. Therm. Sci. 170 (2021) 107091.
[27] Q. Xu, E. Brown, H.M. Jaeger, Impact dynamics of oxidized liquid metal drops, Phys. Rev. E. 87 (2013) 043012.
[28] M.J. Assael, A.E. Kalyva, K.D. Antoniadis, R. Michael Banish, I. Egry, J. Wu, E. Kaschnitz, W.A. Wakeham, Reference data for the density and viscosity of liquid copper and liquid tin, J. Phys. Chem. Ref. Data. 39 (2010) 033105.
[29] Ritwik, Measuring the Viscous Fow Behaviour of Molten Metals under Shear, in, Brunel University, United Kingdom, 2012, pp. 92–105.
[30] Z.F. Yuan, K. Mukai, K. Takagi, M. Ohtaka, W.L. Huang, Q.S. Liu, Surface tension and its temperature coefficient of molten tin determined with the sessile drop method at different oxygen partial pressures, J. Colloid Interface Sci. 254 (2002) 338–345.
[31] T.W. Chapman, The heat capacity of liquid metals, Mater. Sci. Eng. 1 (1966) 65–69.
[32] L. Sun, J. Venart, R. Prasad, The thermal conductivity, thermal diffusivity, and heat capacity of gaseous Argon, Int. J. Thermophys. 23 (2002) 357–389.
[33] H.M. Krutka, R.L. Shambaugh, D.V. Papavassiliou, Effects of die geometry on the flow field of the melt-blowing process, Ind. Eng. Chem. Res. 42 (2003) 5541–5553.
[34] C. Zuniga-Navarrete, C. Zhou, H. Sun, L.J. Segura, Model calibration in inkjet printing process, Proc. Asme. MSEC2023 18th. (2023). V001T001A025.
[35] J. Huang, L.J. Segura, T. Wang, G. Zhao, H. Sun, C. Zhou, Unsupervised learning for the droplet evolution prediction and process dynamics understanding in inkjet printing, Addit. Manuf. 35 (2020) 101197.
[36] L.J. Segura, Z. Li, C. Zhou, H. Sun, Droplet evolution prediction in material jetting via tensor time series analysis, Addit. Manuf. 66 (2023) 103461.
[37] T. Lee, T.G. Kang, J.S. Yang, J. Jo, K. Kim, B. Choi, D. Kim, Gap adjustable molten metal DoD inkjet system with cone-shaped piston head, J. Manuf. Sci. Eng. 130 (2008) 31113–31116.
[38] A. Inoue, T. Masumoto, T. Ekimoto, S. Furukawa, Y. Kuroda, H.S. Chen, Preparation of Fe-, Co-, and Ni-Based amorphous alloy powders by high-pressure gas atomization and their structural relaxation behavior, Metall. Trans. A. 19 (1988) 235–242.
[39] L.A. Jacobson, J. McKittrick, Rapid solidification processing, Mater. Sci. Eng. R. Rep. 11 (1994) 355–408.
[40] S.K. Pillai, T. Ando, Modeling of the in-flight solidification of droplets produced by the uniform-droplet spray process, Int. J. Therm. Sci. 48 (2009) 1494–1500.
[41] T.W. DAVIES, J.M. BEER, Flow in the wake of bluff-body flame stabilizers, Symp. (Int.) Combust. 13 (1971) 631–638.
[42] V. Tesař, Z. Trávníček, Excitational metamorphosis of surface flowfield under an impinging annular jet, Chem. Eng. J. 144 (2008) 312–316.
[43] H. Sohn, D.Y. Yang, Drop-on-demand deposition of superheated metal droplets for selective infiltration manufacturing, Mater. Sci. Eng. A. 392 (2005) 415–421.
[44] S. Schiaffino, A.A. Sonin, Molten droplet deposition and solidification at low Weber numbers, Phys. Fluids 9 (1997) 3172–3187.
[45] C. Clanet, C. Béguin, D. Richard, D. Quéré, Maximal deformation of an impacting drop, J. Fluid. Mech. 517 (2004) 199–208.
[46] T. Mao, D.C.S. Kuhn, H. Tran, Spread and rebound of liquid droplets upon impact on flat surfaces, Aiche J. 43 (1997) 2169–2179.
[47] J. Žunić, K. Hirota, P.L. Rosin, A Hu moment invariant as a shape circularity measure, Pattern Recogn. 43 (2010) 47–57.
[48] M. Ming, X. Wei, X. Shu, H. Zhang, Producing solder droplets using piezoelectric membrane-piston-based jetting technology, J. Mater. Process. Technol. 263 (2019) 233–240.
[49] F.M. White, Fluid Mechanics, McGraw-Hill, New York, 1994, pp. 325–381.
[50] S.D. Hoath, Fundamentals of Inkjet Printing: the science of inkjet and droplets, John Wiley & Sons, 2016, pp. 445–449.
[51] X. Tian, H. Zhao, H. Liu, W. Li, J. Xu, Liquid entrainment behavior at the nozzle exit in coaxial gas–liquid jets, Chem. Eng. Sci. 107 (2014) 93–101.
[52] K. Sidi-Ali, R. Gatignol, Interfacial friction factor determination using CFD simulations in a horizontal stratified two-phase flow, Chem. Eng. Sci. 65 (2010) 5160–5169.